1-12-2024

Structural Basis for Nuclear Import of Hepatitis B Virus (HBV) Nucleocapsid Core

Ruoyu Yang
Thomas Jefferson University

Ying-Hui Ko

Fenglin Li
Thomas Jefferson University

Ravi K. Lokareddy

Chun-Feng David Hou
Thomas Jefferson University

Recommended Citation

Authors

Ruoyu Yang, Ying-Hui Ko, Fenglin Li, Ravi K. Lokareddy, Chun-Feng David Hou, Christine Kim, Shelby Klein, Santiago Antolínez, Juan F. Marín, Carolina Pérez-Segura, Martin F. Jarrold, Adam Zlotnick, Jodi A. Hadden-Perilla, and Gino Cingolani

STRUCTURAL BIOLOGY

Structural basis for nuclear import of hepatitis B virus (HBV) nucleocapsid core

Ruoyu Yang[1], Ying-Hui Ko[2], Fenglin Li[1], Ravi K. Lokareddy[2], Chun-Feng David Hou[1], Christine Kim[3], Shelby Klein[4], Santiago Antolínez[5], Juan F. Marín[5], Carolina Pérez-Segura[5], Martin F. Jarrold[4], Adam Zlotnick[3], Jodi A. Hadden-Perilla[5]*, Gino Cingolani[2]*

Nuclear import of the hepatitis B virus (HBV) nucleocapsid is essential for replication that occurs in the nucleus. The ~360-angstrom HBV capsid translocates to the nuclear pore complex (NPC) as an intact particle, hijacking human importins in a reaction stimulated by host kinases. This paper describes the mechanisms of HBV capsid recognition by importins. We found that importin α1 binds a nuclear localization signal (NLS) at the far end of the HBV coat protein Cp183 carboxyl-terminal domain (CTD). This NLS is exposed to the capsid surface through a pore at the icosahedral quasi-sixfold vertex. Phosphorylation at serine-155, serine-162, and serine-170 promotes CTD compaction but does not affect the affinity for importin α1. The binding of 30 importin α1/β1 augments HBV capsid diameter to ~620 angstroms, close to the maximum size trafficable through the NPC. We propose that phosphorylation favors CTD externalization and prompts its compaction at the capsid surface, exposing the NLS to importins.

INTRODUCTION

Chronic infection by hepatitis B virus (HBV) endangers ~300 million people globally and results in ~800,000 deaths annually (*1*). HBV is localized to the liver and may develop into cirrhosis and carcinoma. Although a vaccine is available, there are no effective drugs to eliminate HBV chronic infection because of the virus' high persistence in the liver (*2*). Thus, a deeper understanding of the HBV life cycle is required to identify new pharmacological targets and develop novel therapeutics.

HBV, the prototypical member of the Hepadnaviridae family, consists of an outer lipid envelope studded with surface protein surrounding an icosahedral nucleocapsid core that contains a partially double-stranded DNA genome (*3*). HBV surface protein recognizes the sodium taurocholate cotransporting polypeptide as its receptor. The virion enters cells via clathrin-mediated endocytosis, is transported in the endosomal network, and escapes endosomes by an incompletely understood mechanism. Localization of HBV to late endosomes is crucial for the productive fusion of the virion lipid membrane to the endosome, releasing the nucleocapsid core in the cytoplasm (*4*). The nucleocapsid comprises a ~36-nm icosahedron with triangulation number *T* = 4, built by 240 copies of the core protein, Cp183 (*5*). HBV replication requires trafficking the entire nucleocapsid to the nuclear pore complex (NPC) into the cell nucleus (*6*). Four arginine-rich motifs in the 34-residue C-terminal domain (CTD) of Cp183 have nuclear localization signal (NLS) activity and are responsible for HBV core nuclear import (*7*–*9*). Nuclear translocation of HBV core particle depends on the host

nuclear import machinery, and phosphorylation of the C terminus of the core protein Cp183 allows HBV capsid to dock to the NPC in an importin-mediated pathway (*10*, *11*).

Phosphorylation of HBV capsid protein affects many aspects of the virus life cycle (*12*). HBV capsid is phosphorylated mainly in the CTD at residues S155, S162, and S170 (*13*–*19*). In addition to playing a role in the nuclear import of HBV nucleocapsid (*10*, *11*), CTD phosphorylation is also linked to the progression of reverse transcription (*20*), pregenomic RNA encapsidation (*14*–*17*, *19*), capsid stability and CTD exposure (*13*), and stabilization of electrostatic interactions inside the capsid (*21*). HBV capsid phosphorylation may occur on the capsid exterior or before assembly. Empty capsids (ECs) are notably hyperphosphorylated (*22*). Multiple host kinases have been implicated, including protein kinase C, serine arginine protein kinase (SRPK), cyclin-dependent kinase 2 (CDK2), and Polo-like-kinase 1 (PLK1), of which only SRPK and CDK2 were confirmed to phosphorylate S155, S162, and S170 in the CTD (*23*). SRPK binds the HBV capsid at the quasi-sixfold vertex, which supports a model where SRPK phosphorylates serines when CTD is exposed through the quasi-sixfold pores (*24*). However, overexpression of SRPK down-regulates the replicated HBV DNA without affecting the RNA level, suggesting that SRPK plays a posttranscriptional role (*25*). Inhibiting CDK2 did not notably affect viral replication (*26*). CDK2 functions as a primer for a second round of phosphorylation performed by PLK1 (*27*) at S168, S176, and S178, which serve as positive effectors of HBV replication (*28*). Evidence also shows that dephosphorylation occurs during pregenome encapsidation or maturation (*22*, *29*), perhaps via a host phosphatase packaged by HBV. In agreement with this idea, Cp183-CTD phosphorylation at S155, S162, and S170 decreases the Cp183-CTD function as a nucleic acid chaperone that binds to the viral DNA via basic residues (*30*).

Nuclear import of cytoplasmic cargos bearing a classical NLS is an energy-dependent process that requires the receptor importin β1 and its adaptor importin α1 (*31*, *32*). Importin α1 makes direct contact with the cargo by accommodating the NLS at its major and/or minor binding site (*33*, *34*) and interacts with importin β1 via the

[1]Department of Biochemistry and Molecular Biology, Thomas Jefferson University, 1020 Locust Street, Philadelphia, PA 19107, USA. [2]Department of Biochemistry and Molecular Genetics, The University of Alabama at Birmingham, 1825 University Blvd, Birmingham, AL 35294, USA. [3]Department of Molecular and Cellular Biochemistry, Indiana University, Bloomington, Indiana, IN 47405, USA. [4]Department of Chemistry, Indiana University, Bloomington, Indiana, IN 47405, USA. [5]Department of Chemistry and Biochemistry, University of Delaware, Newark, DE 19716, USA.
*Corresponding author. Email: gcingola@uab.edu (G.C.); jhadden@udel.edu (J.A.H.-P.)

importin β binding domain (IBB) (*35*). The trimeric complex is then carried into the nucleus, where importin β1 binds to RanGTP with a high affinity, triggering a conformational change that releases the import cargo (*36*). Most cellular cargos are proteins with a size rarely exceeding 0.5 MDa, but the NPC also allows the import of large particles (*37*). Several viruses translocate through the NPC and uncoat in the nucleus, where replication occurs (*38*). Among them are icosahedral DNA viruses such as HBV and rod-shaped baculovirus and RNA viruses such as cone-shaped HIV (*39*). Phosphorylation in the proximity of an NLS has been shown to modulate nuclear import for both cellular and viral cargos (*40*). For instance, the nuclear factor of activated T cells is retained in the cytoplasm by phosphorylation in its NLS. In contrast, nuclear import of the simian virus 40 T-large antigen is stimulated by phosphorylation upstream of the NLS. Phosphorylation of the Epstein-Barr virus nuclear antigen 1 results in both up- and down-regulation of nuclear import, suggesting a dynamic and tunable control of nuclear import by phosphorylation. In the case of HBV nucleocapsid, phosphorylation of the CTD is essential for capsid nuclear import by a mechanism that has remained unknown for nearly three decades (*10*, *11*).

This paper comprehensively analyzes how importin α1/β1 recognizes the HBV EC devoid of nucleic acid. Our data shed light on the location and recognition of the HBV-NLS, the stoichiometry of the EC import complex, and the poorly understood role of phosphorylation in HBV nuclear import.

RESULTS

The adaptor importin α1 bridges HBV capsid to the receptor importin β1

The association of importin β1 with purified HBV EC has been studied in vitro (*41*), but in cell lines, both the adaptor importin α1 and the receptor β1 are required for efficient HBV nuclear import (*10*, *11*). Therefore, we set off to determine whether importin β1 is necessary and sufficient for high-affinity binding to HBV EC or whether the adaptor importin α1 bridges HBV capsid to importin β1. We purified recombinant importins (fig. S1, A and B), along with Cp183 that we assembled into EC (fig. S1C). The EC was titrated against increasing quantities of purified importin α1/β1 heterodimer, individual importin α1 lacking the autoinhibitory IBB (ΔIBB–Imp α1) (*42*), or importin β1 and the resulting mixture analyzed by native agarose gel electrophoresis (Fig. 1, A to C). We found that 20 to 40× molar excess (with respect to the concentration of 240-subunit capsid) of importin α1/β1 was sufficient to entirely shift the migration of EC, giving rise to an intermediate band (Fig. 1A, lanes 8 and 9). In contrast, a vast excess of ΔIBB–Imp α1, as great as 160×, was necessary to fully saturate 1× EC (Fig. 1B, lane 11), displaying a new band with enhanced mobility. EC could also associate with excess importin β1 alone, although the reaction did not reach saturation, suggesting a weak, nonspecific interaction (Fig. 1C, lanes 7 to 11).

To accurately quantify how many copies of the importin α1/β1 heterodimer can associate with one EC, we conducted charge detection mass spectrometry (CD-MS) experiments. CD-MS is a single-molecule technique capable of resolving complex mixtures of particles in the kilodalton to megadalton mass range (*43*). The mass of HBV EC, ~5.23 MDa (Fig. 2A), was increased to ~10.15 MDa in the presence of a 160× excess of importin α1/β1 (Fig. 2B), suggesting that most EC bound to ~30 copies of the 160-kDa importin α1/

β1 complex. The charge distribution is consistent with a compact structure for EC, where charge is clustered at the Rayliegh limit (the expected charge for a spherical molecule), and a more extended structure for importin-decorated particles. Previous CD-MS experiments determined that HBV EC engulfs importin β1 alone in copious amounts (*41*), as also suggested by native gel electrophoresis (Fig. 1C). Thus, native agarose gel electrophoresis and CD-MS confirmed that the importin α1/β1 heterodimer has the highest specificity for EC and forms a regular complex. Namely, 30 copies of importin β1 can associate with one HBV capsid via the adaptor importin α1.

HBV capsid protein contains a C-terminal monopartite NLS

To identify the functional HBV-NLS recognized by importin α1, we crystallized ΔIBB–Imp α1 in complex with a peptide encompassing Cp183-CTD residues 150 to 178 that contain four arginine-rich boxes (Fig. 3A). We solved a structure of ΔIBB–Imp α1:HBV-NLS complex by molecular replacement and refined the atomic model to a $R_{work/free}$ of 18.4/21.4% at 2.0-Å resolution (Table 1). The crystal structure revealed that the HBV-NLS binds to importin α1 at the major binding pocket as a monopartite NLS (Fig. 3B). Spurious

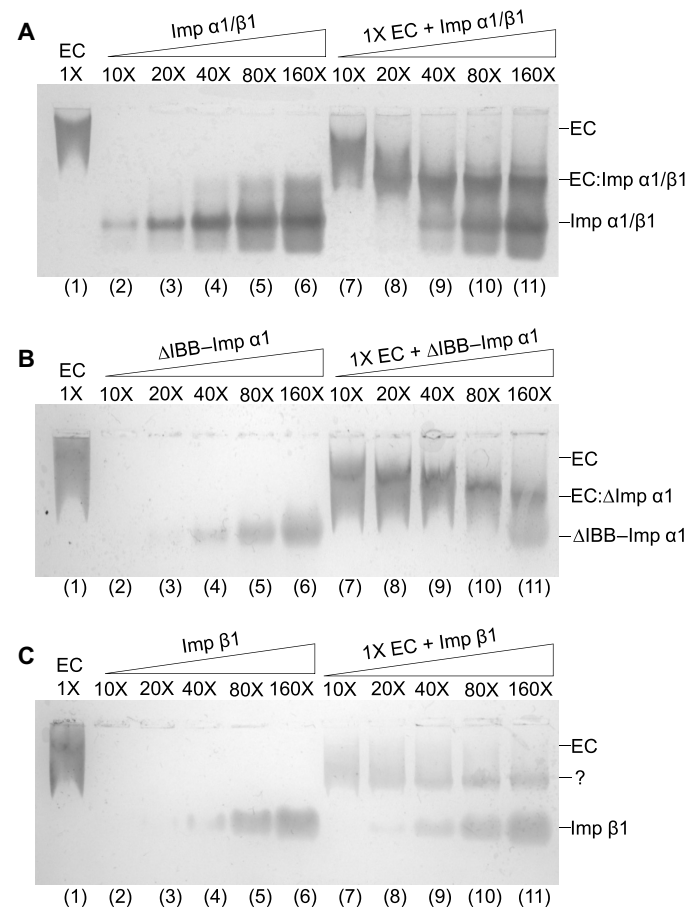**Fig. 1. Binding of purified importins to HBV EC by native agarose gel electrophoresis.** Purified EC was incubated with an excess of the importin α1/β1 heterodimer (**A**) or individually purified ΔIBB–Imp α1 (**B**) and importin β1 (**C**).

density was visible at the minor NLS site at low contour, possibly reflecting excess peptide picked up in the crystallization droplet. Ten Cp183 residues spanning 168-SQSPRR_RRSQ-177 had clear electron density at the major site (Fig. 3B), while no density was observed for the N-terminal residues 150 to 167, which, we conclude, are not part of this NLS. Notably, Cp183 R173 occupies the conserved position P_2 in the NLS, with the guanidinium group visible in two equally populated conformations (Fig. 3B), possibly mimicking a lysine commonly found at this position (33, 34). Cp183 residues at P_1, P_3, and P_4 are also arginines, again a rather unusual feature distinct from classical NLSs. The refined B factor for Cp183-NLS residues at the major site is 50.4 $Å^2$, similar to importin $\alpha1$ (~41.5 $Å^2$) (Table 1). The association between the HBV-NLS and importin $\alpha1$ is mainly stabilized by contacts between Cp183 residues 172-RRRR-175 (P_1 to P_4) and importin $\alpha1$ major NLS pocket, including 22 hydrogen bonds and three salt bridges (Fig. 3C). The most commonly phosphorylated sites in Cp183, S155, S162, and S170 (red in Fig. 3A), do not appear to make important contacts with importin $\alpha1$. S155 and S162 were disordered in the crystal structure, and S170, at position P_{-1} makes only one hydrogen bond with W231 (Fig. 3C).

A previous study found that a peptide representing core protein amino acids 156 to 166 (PRRRTPSPRRR) facilitated efficient nuclear transport, while a peptide representing amino acids 163 to 173 (PRRRRSQSPRR) showed only a poor import reaction (fig. S2A) (9). These data can be reconciled with our HBV-NLS crystal structure and suggest the minimal motif for importin $\alpha1$–mediated nuclear entry of HBV. The first sequence, although associated with a portion of the CTD upstream of our crystallized NLS (SQSPRRRRSQ), contains a similar motif TPSPRRR (fig. S2B), where T provides a chemically suitable substitution for S168, and P can satisfy the observed backbone conformation of Q169 ($\phi = -75°$), whose side chain only makes one hydrogen bond with the adaptor. The second sequence overlaps the NLS identified in our crystal but, despite two possible alignments, does not contain a complete binding motif, as either the preceding SQS or terminal R residue (P_4) that makes five contacts in the crystal structure (Fig. 3C) is missing (fig. S2C). These results suggest that the minimal NLS sequence is SQSPRRRR, corresponding to amino acids 168 to 175, in agreement with our crystal complex. Thus, Cp183 NLS lies at the far C-terminal end of the capsid protein between amino acids 168 to 175 and binds exclusively to the major NLS site of importin $\alpha1$.

Cryo–electron microscopy reconstructions of HBV EC in the presence of importins

To investigate how importins associate with HBV EC, we determined cryo–electron microscopy (EM) reconstructions of HBV EC alone and in complex with ΔIBB–Imp $\alpha1$ and importin $\alpha1/\beta1$ heterodimer using single-particle analysis (SPA) (Table 2 and figs. S3 and S4). A 3.0-Å reconstruction of EC (Fig. 4A) revealed visible pores between neighboring subunits and a hollow interior devoid of the genome. Previous work found that EC can nonspecifically engulf importin $\beta1$ (~97 kDa) (41), pointing to extreme capsomer plasticity. In agreement with this idea, the reconstruction of EC with
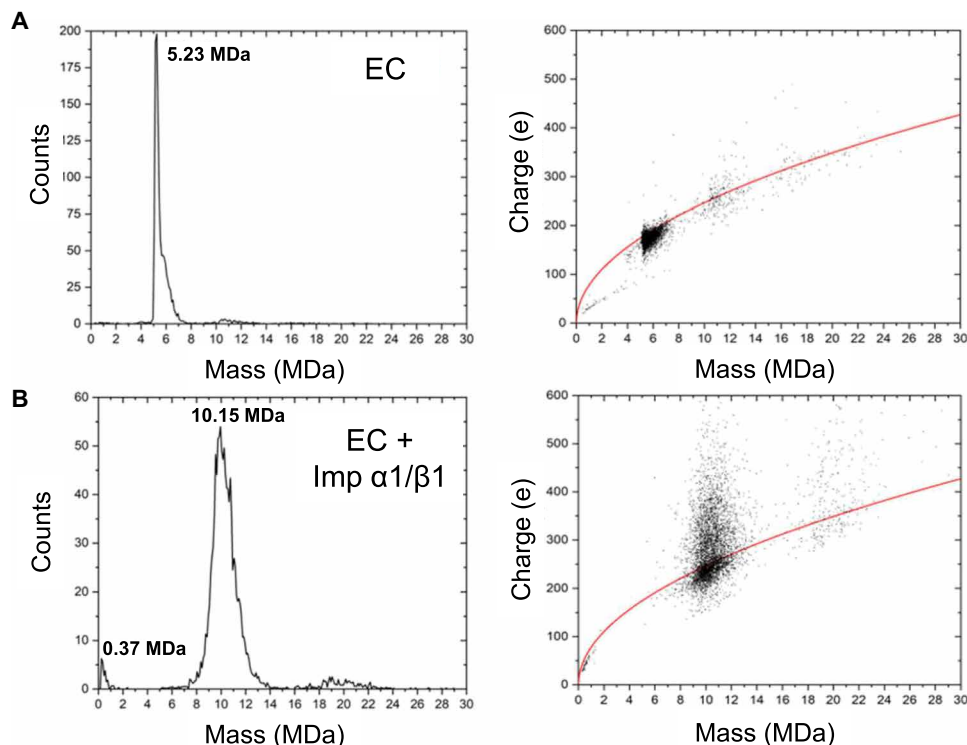
Fig. 2. Binding stoichiometry between EC and the importin α/β1 heterodimer determined by CD-MS. (**A**) EC peaked at 5 MDa, while (**B**) the EC:importin α1/β1 complex was detected at 10.15 MDa, which is consistent with one capsid bound to 30 copies of the ~160-kDa importin α1/β1 heterodimer. The charge distribution for ions (right column) is consistent with a compact structure for EC where the ion distribution is close to the Rayleigh limit (red line) and a much less compact structure for importin-decorated capsids.

an excess of ΔIBB–Imp α1 had continuous density inside the capsid that we ascribed to nonspecifically engulfed ΔIBB–Imp α1 (~55 kDa) (Fig. 4B). This reconstruction explains the superstoichiometric association of a ~160× molar excess of ΔIBB–Imp α1 with EC probed by native agarose gel electrophoresis (Fig. 1B). In contrast, a reconstruction of EC bound to importin α1/β1, resolved to 3.4-Å Fourier shell correlation (FSC) resolution, revealed 30 discrete densities decorating the capsid surface at the icosahedral twofold (quasi-sixfold) axes (Fig. 4C). The number of noncapsid densities visible in the reconstruction agrees with the estimated number of importin α1/β1 heterodimers bound to EC observed by native gel electrophoresis (Fig. 1A) and CD-MS (Fig. 2B), suggesting that each density at the quasi-sixfold represents one importin

Fig. 3. Crystal structure of HBV-NLS bound to ΔIBB–Imp α1. (**A**) A ribbon diagram of dimeric Cp183 showing the amino acid sequence for the unresolved CTD. Four arginine-rich boxes are underlined with arginines and phosphoacceptors colored in black and red, respectively. (**B**) The crystal structure of ΔIBB–Imp α1 (shown as a yellow solvent surface) bound to the HBV-NLS (in green sticks) refined at 2.0-Å resolution. A magnified view of the HBV-NLS overlaid to the experimental Fo-Fc electron density contoured at 2σ shows that the guanidinium group of R173 at the P₂ site exists in two conformations. (**C**) Schematic diagram of all major contacts between HBV-NLS and ΔIBB–Imp α1 observed at the major NLS binding site. Hydrogen bonds and salt bridges are shown as dashed black and green lines. A red frame highlights R173 at the P₂ position.

α1/β1 complex. In addition, no random density was observed inside the capsid (Fig. 4C), indicating that the importin α1/β1 heterodimer is not readily engulfed.

One NLS per quasi-sixfold is sufficient to bind importin α1
We built the icosahedral asymmetric unit of EC, EC:ΔImp α1, and EC:Imp α1/β1, each composed of four Cp183 monomers and subjected all atomic models to real space refinement (Table 2). The full capsids were built by applying icosahedral symmetry and then compared. We found that EC incubated with a 160-fold molar excess of ΔIBB–Imp α1 (Fig. 1B, lane 11) was expanded by 17 Å (fig. S5A), and EC bound to 30 copies of importin α1/β1 was also slightly larger (~8 Å) than wild-type (WT) EC (fig. S5B). Importin α1 is very acidic (isoelectric point, ~4.5), and so is importin β1 (isoelectric point, ~4.7), while the inner surface of HBV capsids (lacking or extruding CTDs to the outside) is mildly basic (*19*), suggesting that electrostatic forces that drive the nonspecific engulfment of individual importins also cause transient capsid rupture.

We next focused on the HBV quasi-sixfold channel, where the density for importin α1/β1 was observed in the cryo-EM reconstruction (Fig. 4C). A pore of varying diameter between 9 and 13 Å is visible at the quasi-sixfold (fig. S6A) (*44*). In section view, the last Cp183-CTD residue resolved in the density was G153, while the functional NLS (residues 168 to 175) was invisible, likely because of its structural flexibility. A portion of the CTD (residues 150 to 153) was built by tracing the density extending from one of the six chains that form the hexameric pore. The remaining Cp183 residues, including the NLS, were modeled as projecting outside the capsid (fig. S6B). The narrow size of the quasi-sixfold pore makes it unlikely for more than one CTD to thread through (*44*), suggesting only one NLS per hexamer protrudes outside the capsid, totaling 30 NLSs per nucleocapsid core. This stoichiometry agrees with the major population observed by CD-MS with a mass consistent with 30 copies of importin α1/β1 bound to one EC, one importin complex per quasi-sixfold (Fig. 2B).

Importin α1 decorates the HBV capsid, while importin β1 is highly mobile
We generated a difference map for importin α1/β1 by subtracting the density for EC from the EC:Imp α1/β1 map, which yielded 30 cauliflower-shaped blobs. The central blobby density was masked and subjected to localized three-dimensional (3D) classification and refinement (fig. S3) that gave an arched density laying on top of the quasi-sixfold pore, positioned with the concave surface facing the capsid (Fig. 5A). This density resembles the N terminus of importin α1, corresponding to Armadillo (Arm) repeats 1 to 5. In contrast, importin β1 is not visible in the EC:Imp α1/β1 reconstruction, likely because it moves around the HBV-tethered importin α1 core with high frequency, which makes it impossible to align for SPA. Although limited in resolution, the reconstruction gave us sufficient structural restraints to fit the crystal structure of importin α1:HBV-NLS (residues 168 to 177) inside the arched density and determine the position of the Cp183 NLS with respect to the capsid surface. We also modeled the missing residues in the CTD not visible in the reconstruction (Fig. 5B). This structural model suggests that Cp183 CTD emerging from the quasi-sixfold pore folds back toward the capsid surface to position the NLS antiparallel to importin α1 Arm core.

To confirm that the density seen above the quasi-sixfold pore corresponds to importin α1 instead of importin β1, we bound HBV
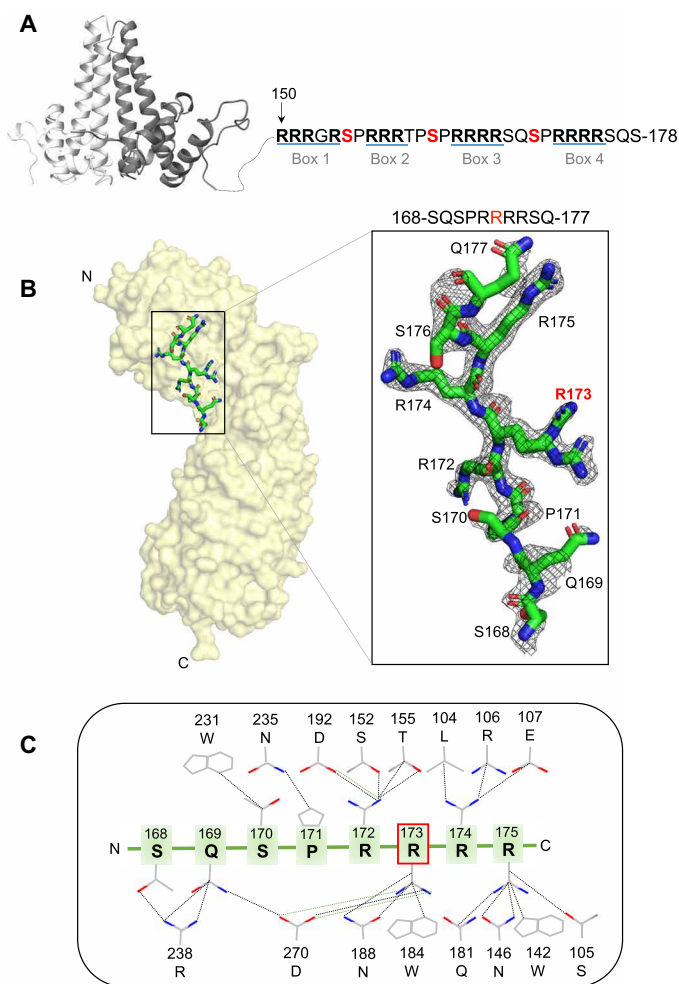
Table 1. Crystallographic data collection and refinement statistics. Values in parentheses are for the highest-resolution shell.

	HBV-NLS:ΔIBB–Imp α1
Data collection	
Beamline	SSRL 12-1
Wavelength (Å)	0.976
Space group	$P2_1 2_1 2_1$
Cell dimensions	
a, b, c (Å)	78.4, 90.7, 97.2
α, β, γ (°)	90.0, 90.0, 90.0
Reflections (tot/unique)	343,307/47,594
Resolution (Å)	50.0–2.0 (2.06–1.99)
Completeness (%)	98.8 (99.3)
Redundancy	3.4 (3.4)
Rsym	5.2 (73.9)
Rpim	3.3 (60.5)
$I/\sigma I$	22.5 (1.5)
Wilson B factor (Å^2)	34.2
Refinement	
PDB entry	7UMI
Resolution limits (Å)	41.09–1.99
No. of reflections	47,537
R_{work}/R_{free}*	18.4/21.4
No. of protein atoms	3313
No. of solvent molecules	274
B factor (Å^2)	
Importin α1/NLS	41.5/50.3
Waters	45.7
Ramachandran plot (%)	
Core allow/gen. allow/disallow	98.4/1.4/0.2
Root mean square deviations from ideal	
Bond lengths (Å)	0.008
Bond angles (°)	0.95
MolProbity/clash score	1.2/4.0

*The R_{free} value was calculated using ~2000 randomly selected reflections.

EC to ΔIBB–Imp α1 fused to an N-terminal maltose binding protein (MBP-α1) and imaged EC in the presence of an excess of MBP-α1 and an anti-MBP monoclonal antibody (table S1). A cryo-EM reconstruction of the EC:MBP-α1:antibody complex revealed 30 copies of density at the quasi-sixfold pores similar to that observed with the full-length importin α1/β1 heterodimer (fig. S7). Thus, cryo-EM difference analysis confirmed that the density bound to the HBV capsid corresponds to importin α1.

The importin α1/β1 heterodimer is intrinsically flexible

To rationalize why importin β1 is not visible in the EC:Imp α1/β1 reconstruction, we also studied the purified importin α1/β1 heterodimer without NLS cargo using cryo-EM SPA. A homogeneous importin α1/β1 heterodimer was purified using a histidine (his)–tag in importin α1 (*45*), avoiding unwanted degradation (Fig. 6A). The importin α1/β1 heterodimer was vitrified on carbon-coated grids, and ~8000 high-quality micrographs were acquired using a 300-kV

Krios microscope equipped with Gatan K3 direct detector (Table 2). Approximately 1 million picked particles were used to compute 2D class averages that revealed the snail-like shape of importin β1 (Fig. 6B) (*46*). A further round of 3D refinement yielded a 3.95-Å density map (Fig. 6C) with clear features for importin β1 and the IBB domain of importin α1 (residues 1 to 54) but no density C-terminal of residue 55. The lack of density for the importin α1 Arm core suggests that this part of the importin complex exists in infinite poses, preventing classification into one or few homogenous classes, as required for SPA. An atomic model of the importin β1:IBB complex was built by docking the crystal structure into the density and subjected to real-space refinement (Fig. 6D and Table 2). Cryo-EM and x-ray (*46*) models are essentially identical (root mean square deviation = 1), confirming the rigidity of importin β1 when bound to the IBB.

The amino acid sequence between the end of importin α1's IBB and the beginning of the well-folded Arm core, residues 53 to 77,

Table 2. Cryo-EM data collection, map, and model refinement statistics.

Data collection		EC	EC:ΔIBB–Imp α1	EC:Imp α1/β1	Imp α1/β1
Facility/microscope		NCCAT/ Titan Krios	NCEF/Titan Krios		
Camera			Gatan K3		
Magnification			81,000		105,000
Voltage (kV)			300		
Electron exposure (e⁻/Å²)			50		
Defocus range (μm)		−0.8 to −2	−0.5 to −1.5	−0.75 to −2.0	−0.8 to −2.4
Pixel size (Å)		0.53 (1.06)	0.56 (1.12)	0.56 (1.12)	0.44 (0.88)
Total movies (frames per movie)		10,015 (40)	8,352 (40)	6,653 (40)	8,778 (40)
Initial particle images (no.)		564,330	238,953	85,666	1,512,111
Final particle image (no.)		23,919	37,698	16,181	1,009,142
Processing and refinement					
PDB entry code		8G5V	8G8Y	8G6V	8GCN
Symmetry		I3	I4	I2	C1
Model		Hexamer	Hexamer	Hexamer	Heterodimer
Map resolution (Å)		3.0	3.8	3.4	3.95
FSC threshold		0.143	0.143	0.143	0.143
Initial model (PDB code)		1QGT	1QGT	1QGT	1QGK
Correlation coefficient		0.84	0.89	0.89	0.83
Model composition	No. of chains	12	12	12	3
	Non-H atoms	13,739	13,717	13,736	7178
	Residues	1718	1715	1716	919
Root mean square deviations	Bond lengths (Å)	0.004 (0)	0.003 (0)	0.003 (0)	0.004 (0)
	Bond angles (°)	0.609 (2)	0.568 (2)	0.595 (5)	0.751 (3)
Validation	MolProbity score	1.57	1.31	1.42	2.15
	Clash score	7.56	5.66	5.65	25.87
	Rotamer outliers (%)	0.00	0.53	0.59	0.51
Ramachandran plot	Favored (%)	97.11	98.82	97.46	96.28
	Allowed (%)	2.89	1.18	2.54	3.72
	Outliers (%)	0.00	0.00	0.00	0.00

has low complexity and is predicted to be unstructured (Fig. 6E). Accordingly, this linker is readily cleaved by proteases in vitro (*47*). The linker allows the Arm core to move around the rigid importin β1:IBB complex, explaining the lack of Arm-core density in the cryo-EM reconstruction of the isolated importin α1/β1 complex (Fig. 6D). To reduce the flexibility between importin α1 and β1, we genetically removed residues 53 to 76 from importin α1, purified the importin Δ53–76–α1/β1 complex, and carried out cryo-EM analysis in complex with HBV EC. Although the solubility of this engineered importin complex was reduced, we obtained a medium-resolution cryo-EM reconstruction that, when compared to the WT EC:Imp α1/β1 reconstruction at the same resolution and contour, had a much-reduced density around the quasi-sixfold pore (Fig. 6, F and G). The cauliflower-shaped density seen for the full-length importin α1/β1 complex likely represents an average of all possible conformations importin β1 adopts around the HBV capsid when tethered to the NLS by importin α1 (Fig. 6F). Removing the flexible linker in importin α1 made the density much smaller and thinner (Fig. 6G), suggesting that importin β1 becomes sterically restrained.

However, the density was poorly resolved because of remaining flexibility in the importin α1/β1 heterodimer that is difficult to align during SPA.

Phosphorylation upstream of the NLS enhances CTD compactness

Cytoplasmic HBV nucleocapsids are heavily and heterogeneously phosphorylated (*48*, *49*), although maturation apparently reduces the phosphate content in DNA-filled cores (*22*, *29*). Nuclear import has been shown to depend on phosphorylation of the CTD (*10*, *11*), but the mechanistic role of phosphorylation, including the function of specific modification sites, is unknown. Although the CTD contains seven possible phosphorylation sites, S155, S162, and S170 are modified most frequently. In principle, the majority of CTD between residues 150 and 183 can be exposed to the capsid exterior, and phosphorylation can be expected to affect NLS presentation. Assuming a fully extended conformation, the CTD would project about 85 Å from the capsid floor, with an estimated radius of gyration (Rg) of 27 Å (Fig. 7A, left). In contrast, the NLS modeled in the

cryo-EM reconstruction of HBV bound to importin α1/β1 is only 39 Å above the capsid floor, corresponding to an Rg of ~15 Å (Fig. 7A, right). To explore the relationship between phosphorylation and NLS recognition, we performed all-atom molecular dynamics (MD) simulations of the CTD (residues 150 to 183) in the unphosphorylated and S155, S162, and S170 phosphorylated states. Conformational sampling used the Anton 2 computer and totaled 30 μs per system. MD simulation results indicate that the addition of these phosphates causes the CTD to adopt a more compact conformation owing to increased electrostatic contact with its constituent arginines. The conformational space available for the unphosphorylated CTD, characterized by its Rg and end-to-end distance, became restricted upon phosphate modification at S155, S162, and S170 (Fig. 7B). The Rg drops from a maximum of 29.4 Å for the unphosphorylated CTD to 18.9 Å for the phosphorylated, with average values of 17.3 and 11.0 Å, respectively. This means that while both CTD systems sample conformations amenable to the positioning of importin α1/β1 observed in the cryo-EM reconstruction, phosphorylation enhances the stability of states that are more compact to display the NLS close to the capsid surface. Because compaction increases CTD bulk, a CTD phosphorylated on the exterior of a capsid will be trapped on the exterior, and if phosphorylated on the capsid interior, then it will be less likely to escape through the quasi-sixfold pore. Structural compaction is primarily dictated by intrapeptide sidechain contacts between phosphorylated serines and arginines instead of mainchain bonding (fig. S8, A and B).

MD simulations also revealed that compaction induced by CTD phosphorylation at S155, S162, and S170 leads to a concomitant decrease in accessibility of the NLS (Fig. 7C). However, 64.5% of phosphorylated CTD conformers exhibited the minimum solvent-accessible surface area (SASA) required for binding importin α1/β1, such that structural compaction is balanced with favorable presentation of the NLS. Loss of NLS accessibility is driven primarily by electrostatic interactions between S170 and neighboring arginines, which are almost negligible but increase markedly upon phosphorylation (fig. S8B). In particular, a phospho-S170 to R172 salt bridge was observed in over 90% of conformers: This preferred self-interaction could potentially distort the required conformation of the NLS to fit in the importin α1 groove (Fig. 3C), at odds with the stimulatory role of phosphorylation on HBV nuclear import (10, 11).

Phosphorylation near the NLS does not affect importin α1/β1 binding

To test the impact of phosphorylation on NLS recognition, we generated three CTD constructs fused to the C terminus of glutathione S-transferase and encoding WT Cp183 CTD residues 150 to 178 (GST-WT-CTD); CTD lacking the NLS in Box4 (GST-ΔNLS-CTD); CTD with three phosphomimetics at S155E, S162E, and S170E (GST-EEE-CTD). All CTD variants were purified to homogeneity, coupled to glutathione beads, and incubated with a physiological concentration of purified importin α1/β1. After 45 min of incubation, the beads were washed three times and analyzed by SDS–polyacrylamide gel electrophoresis (PAGE) analysis to evaluate the amount of bound importin α1/β1. The experiment was repeated three times to estimate an SD (fig. S9, A and B). This equilibrium pull-down revealed that the triple-phosphomimetics CTD has statistically similar binding to importin α1/β1 as WT GST-CTD ($P = 0.0185$). In contrast, the GST-ΔNLS-CTD has statistically reduced affinity for importin α1/β1 ($P = 0.0017$), in agreement with the loss of a functional NLS. GST-ΔNLS-CTD retained some binding avidity for importin α1/β1, as expected for a 20-residue peptide that contains 11 arginine.

While S155 and S162 lie upstream of the NLS identified crystallographically, S170 is located within the NLS and could affect importin α1 binding via direct contact with the protein. To further explore the relationship between phosphorylation and NLS recognition, we performed MD simulations of the complex in the unphosphorylated state and with phosphate modification at S170 (fig. S10A). Production simulations used the Delta computer and totaled 1.2 μs of aggregate sampling per system. Free energies of binding were computed with the molecular mechanics/generalized Born surface area method (50). Relative to the unphosphorylated state, phosphate modification at S170 had a modest but favorable impact on binding ($\Delta\Delta G = -3.0$ kcal/mol; fig. S10B) resulting from the combined contributions of two distinct conformational states observed in MD simulations (fig. S10C). When phospho-S170 forms an intra-NLS salt bridge with R173 (fig. S10D), the resulting NLS conformation introduces a new hydrogen bond between S168
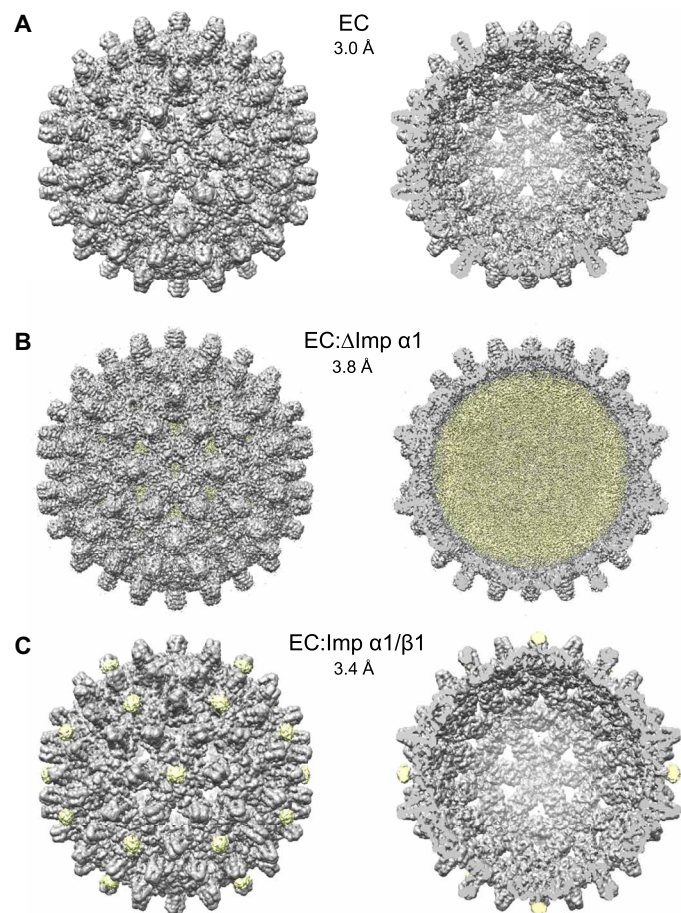

Fig. 4. Cryo-EM analysis of HBV EC bound to human importins. Icosahedral reconstructions of HBV EC (**A**), EC bound to a molar excess of ΔIBB–Imp α1 (**B**), and EC bound to a molar excess of importin α1/β1 (**C**). The three reconstructions were determined at 3.0-, 3.8-, and 3.4-Å FSC resolution, respectively, and are contoured at 2.2 σ. HBV EC is colored gray, while density features ascribed to importins are colored yellow.

and importin α1 D270, replacing the Q169-D270 contact captured in the crystal structure and stabilizing motion of the NLS N terminus. Consistent with predictions based on the CTD in isolation (fig. S8, A and B), when phospho-S170 forms intra-NLS salt bridges with R172/R174 (fig. S10E), the resulting conformation induces local compaction of the NLS, pulling its N terminus out of the groove and eliminating importin α1 R238/D270 contacts. These conformational states increase and decrease binding affinity, respectively. The average $\Delta\Delta G$ value calculated for the system with phosphorylation at S170 is within 0.4σ for their respective distributions, emphasizing the mobility of the NLS in the importin α1 binding groove and its flexibility even when bound. Thus, combining experimental and computational methods, we determined that CTD phosphorylation at the three most commonly modified sites, S155, S162, and S170, does not directly increase or decrease binding affinity for importin α1/β1. Phosphorylation likely induces a structural change in the CTD (e.g., compaction) that indirectly promotes importin α1/β1 recruitment.
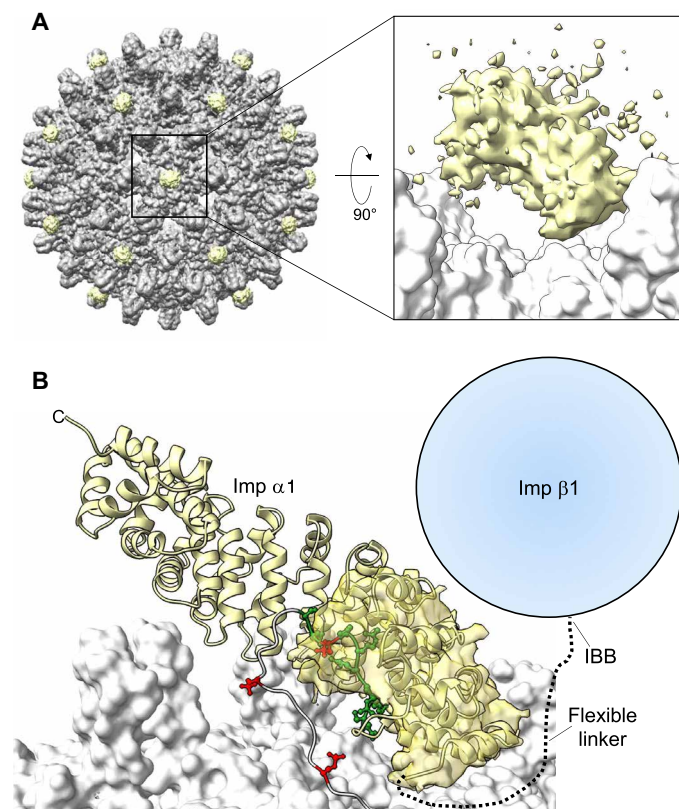

Fig. 5. Importin α1 binds to the HBV-NLS exposed at the quasi-sixfold channel. (**A**) A global view of 30 importin α1/β1 blobs visible around the quasi-sixfold channels of HBV EC. The zoom-in panel shows the arched electron density for importin α1/β1 (yellow) obtained after focused refinement. (**B**) A model of importin α1 (yellow ribbon) docked into the density observed at the quasi-sixfold bound to the HBV-NLS (green stick). Phospho-S155, -S162, and -S170 are colored in red. Importin β1 is schematized as a blue circle connected to importin α1 IBB by a flexible linker (dashed black line).

DISCUSSION

HBV has one of the smallest viral genomes known for a human pathogen, just 3.2 kb of circular, partially double-stranded DNA (*51*). To infect and replicate in human cells, the virus exploits multiple aspects of a cell's molecular machinery, including secretory and exocytic pathways (Fig. 8, i), the endosomal sorting complexes required for transport, autophagy pathways, as well as hijacks importins and uses the RanGTP gradient to enter the cell nucleus (*52*). Consistent with its economical nature, HBV does not encode any protein kinase or other modifying enzymes but uses host kinases to modulate its trafficking inside the host (*53*).

Here, we have delineated the molecular determinants that allow the HBV nucleocapsid core to be transported to the cell nucleus. This reaction requires both importins and cellular kinases, although the interplay between the two has remained elusive. We mapped the functional NLS in HBV Cp183 that spans the most C-terminal of four basic arginine-rich boxes. Cp183 NLS binds the major NLS pocket of importin α1 and is unusually rich in arginine residues: Even the crucial residue at P_2 is an arginine, visible in two conformations in our crystal structure. Combining native gel electrophoresis, CD-MS, and cryo-EM, we demonstrate that preferentially 30 copies of the importin α1/β1 complex decorate HBV's 30 quasi-sixfold vertices. The center of each quasi-sixfold houses a narrow pore, ~9 to 13 Å in diameter, in our cryo-EM reconstruction, from which only one NLS is likely to emerge at any given time. Externalization of capsid protein moieties located inside the capsid that suddenly become surface exposed is not new to HBV but has been described for several other viruses such as poliovirus (*54*), rhinovirus 14 (*55*), swine vesicular disease virus (*56*), and flock house virus (*57*), reflecting the plasticity of capsid proteins. However, unique to HBV biology is the fact that the CTD transiently exposes a functional NLS. Our study provides experimental evidence that importin α1/β1 bind the HBV-NLS as it protrudes from the HBV capsid. The way importin α1/β1 recognizes the arginine-rich NLS is somewhat unexpected. Located at the C-terminal end of the intrinsically disordered CTD (*58*), the NLS could, in principle, extend as much as ~85 Å above the capsid surface. Instead, our cryo-EM reconstruction of the EC:Imp α1/β1 complex showed that importin α1 preferentially collapses onto the quasi-sixfold pore, projecting its concave surface toward the NLS that folds backward to bind importin α1 major NLS-binding site in an antiparallel manner. Heterogeneity of the tolopology of the EC:Imp α1/β1 complex is implicit in the distribution of charge seen in CD-MS. The favored interaction places the NLS at a maximum 39-Å distance from the capsid surface and occurs, while importin β1 is flexibly tethered to the capsid, free to move around the quasi-sixfold. Both the adaptor importin α1 and importin β1 are required for NLS recognition, as individual importin β1 (molecular weight, ~97.5 kDa) (*41*) or importin α1 (molecular weight, ~60 kDa) (Fig. 4B) can be engulfed into the capsid that would prevent nuclear import.

MD simulations of the isolated CTD support our experimental structural data. The unphosphorylated CTD has a distribution of Rg values consistent with an intrinsically disordered protein. However, phosphorylation of S155, S162, and S170 markedly reduced the Rg, inducing structural compaction (e.g., Rg of 11.0 Å on average) consistent with the cryo-EM reconstruction of HBV:Imp α1/β1 complex (Fig. 8, ii). CTD compaction upon phosphorylation is achieved by an intramolecular network of side-chain contacts between phosphate moieties and CTD arginine side chains that latches the CTD
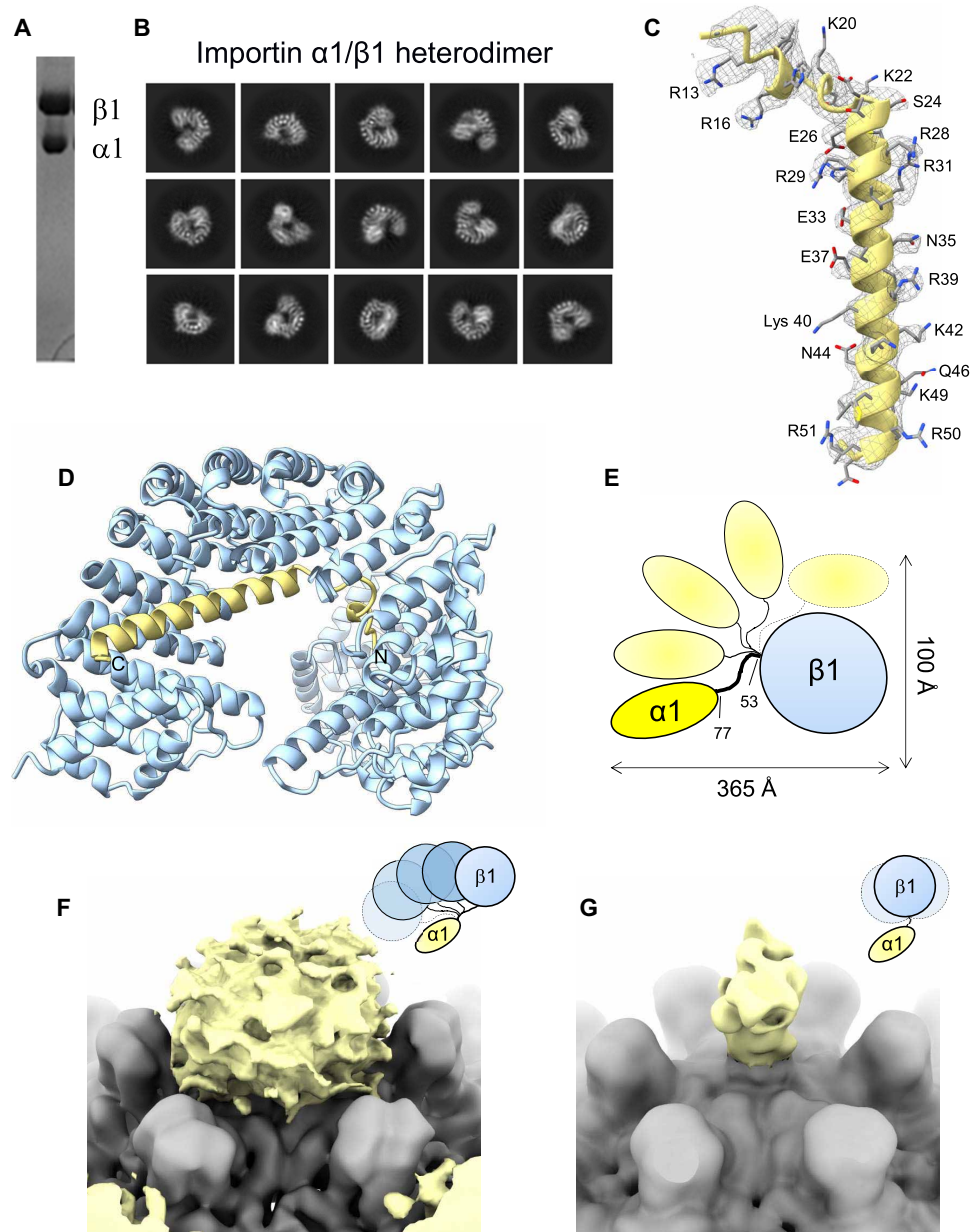
Fig. 6. Cryo-EM single particle analysis of the purified importin α1/β1 heterodimer. (**A**) SDS–polyacrylamide gel electrophoresis (PAGE) analysis of the purified importin α1/β1 heterodimer and (**B**) relative 2D class averages obtained using cryoSPARC. (**C**) Quality of the 3.95-Å cryo-EM density (gray) contoured at 2.2 σ and overlaid with the IBB (yellow). (**D**) Refined atomic models of importin β1 (cyan) bound to the IBB domain (yellow). (**E**) Cartoon model of the importin α1/β1 complex. The flexible linker in importin α1 (residues 53 to 77) is colored in black. Magnified view of WT importin α1/β1 (**F**) and the engineered importin Δ53–76–α1/β1 (**G**) bound to a quasi-sixfold pore. The capsid is colored gray, while the importin is colored yellow. The small cartoon models on the top right illustrate the proposed arrangement of importin α1 (yellow) and β1 (cyan).

polypeptide chains at distinct points, favoring a reduced spatial footprint while maintaining the accessibility of the NLS in the majority of conformers. Our data agree with a recent solid-state nuclear magnetic resonance study, which found that CTD does not form specific secondary structures in the context of RNA binding or upon phosphorylation and that phosphorylated CTDs exhibit restricted motion (*58*). Furthermore, the decrease in conformational space sampled by the CTD upon phosphorylation observed in MD

simulations is consistent with enhanced structural stability due to the introduction of salt bridges. Experimentally, a CTD-fusion protein carrying three phosphomimetics at S155, S162, and S170 has WT binding for importin α1/β1, suggesting that phosphorylation does not enhance or decrease the NLS binding affinity for importins. Previous work showed that HBV capsids containing three phosphomimetics at S155, S162, and S170 (Cp183-EEE) have enhanced stability and exhibit a much slower rate of CTD proteolytic

cleavage compared with WT capsids (13). Thus, we propose that phosphorylation promotes and stabilizes CTD compaction, improving NLS presentation to importins and stimulating HBV nucleocapsid nuclear import (Fig. 8, iii) (10). CTD compaction could slow NLS reinternalization (or inhibit externalization of the CTD), enhancing the window of opportunities for importins to bind the NLS. Importin α1 and β1 are highly abundant in the cytoplasm of eukaryotic cells (~1 to 3 μM) (59), but many other NLS cargos compete for their association (60), so extending the presentation of HBV-NLSs could be advantageous to recruit importins. In addition, CTD phosphorylation reduces the affinity of the capsid protein for the packaged HBV genome inside the capsid, potentially promoting

its externalization (11, 12). Protein kinase activity was found inside hepatitis B virions, possibly via a capsid-trapped kinase (61), suggesting that the CTD could be phosphorylated even before being externalized. After externalization through the quasi-sixfold pore, phosphorylated CTD would be prone to compaction, enhancing its persistence outside the capsid and favoring importin α1/β1–dependent recruitment. Thus, CTD phosphorylation plays a multifaceted role, favoring externalization by reducing intracapsid association with nucleic acids and promoting NLS exposure and presentation to importins after externalization through compaction.

Our analysis of the HBV EC decorated by 30 copies of the flexible importin α1/β1 heterodimer suggests that the total diameter of the
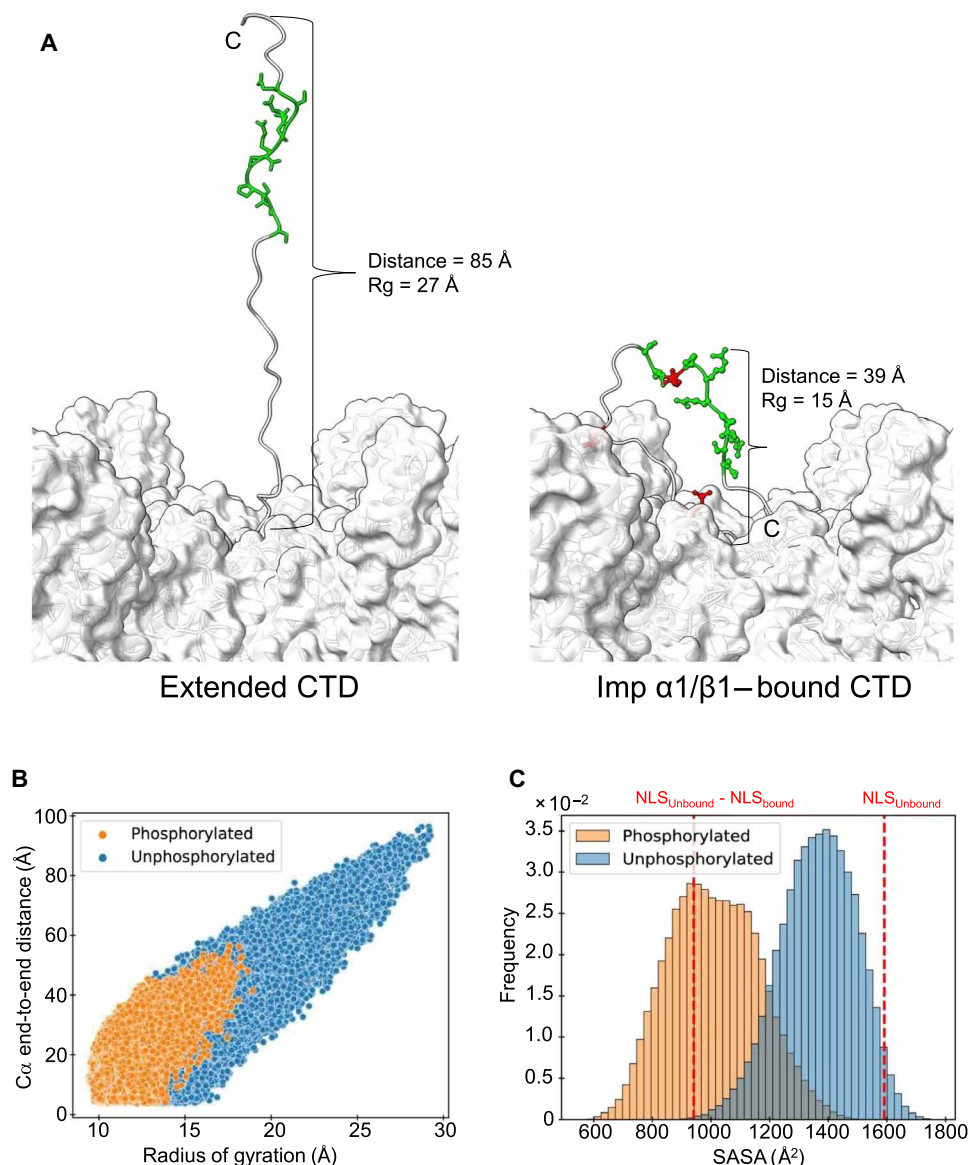

Fig. 7. Role of phosphorylation in CTD. (**A**) Model of CTD residues 150 to 183 emerging at the quasi-sixfold pore assuming (left) an extended conformation that lacks intramolecular bonding; (right) the conformation modeled in complex with importin α1/β1 (Fig. 5B). (**B**) CTD peptide end-to-end distance versus radius of gyration (Rg) and (**C**) NLS SASA distributions for unphosphorylated (orange) and S155, S162, and S170 phosphorylated (blue) states. The minimum NLS SASA required for binding of importin α1/β1 was estimated on the basis of the structure of ΔIBB–Imp α1:HBV-NLS complex by subtracting the SASA of the bound NLS from that of the unbound NLS in its crystallographic conformation.

HBV import complex is close to 62 nm (Fig. 8, iv). One limitation of this study is that we used HBV ECs instead of capsids filled with viral genome. We speculate that nucleic acid–filled capsids have fewer CTDs available for bonding with importins due to the electrostatic interactions between basic CTDs and the acidic genome inside the capsid. Thus, it is possible that, in a cell, only a subset of the 30 available CTDs protrude outside the HBV nucleocapsid, unlike in vitro. Multiple NLSs on a cargo enhance avidity for importins, ensuring faster nuclear import, but are energetically more costly to be displaced upon nuclear entry (37). Thirty importin α1/β1 copies per HBV capsid is likely an upper estimate for unimpeded decoration by importins, a "Vmax" observed using saturating quantities of importins.

CD-MS data show that exceeding 30 α1/β1 copies is disfavored. Is the NPC large enough to accommodate the HBV import complex? The answer to this question comes from recent work on the nuclear import of HIV-1 capsid. Similar to HBV, HIV-1 requires nuclear entry for replication, and its capsid protein carries an NLS recognized by soluble nuclear transport receptors, including Karyopherin β2/Transportin-1 and Transportin-3 (62). Cryo-electron tomography (ET) revealed that the entire 60-nm cone-shaped HIV-1 capsid is translocated through the NPC that dilates to ~64 nm at the inner ring (39). A substantially wider NPC diameter and an increase in the central channel volume by up to 75% were also observed in NPC models obtained from lamellae prepared using cryo–focused ion
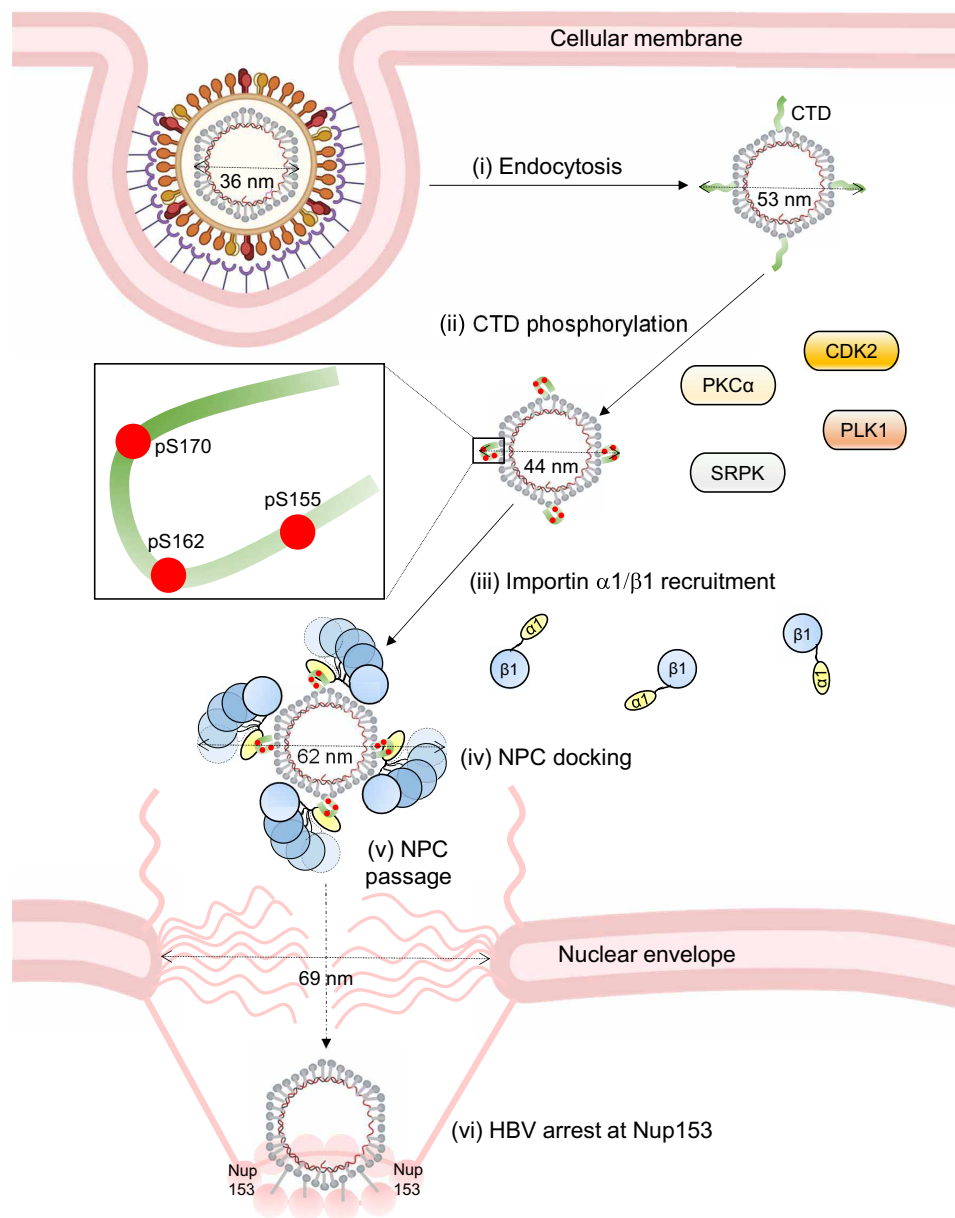

Fig. 8. A model for HBV capsid nuclear import through the NPC. The diameter of the HBV capsid decorated by 30 importin α1/β1 is ~62 nm. The dilated NPC is estimated to be ~69 nm (64). (**i** to **vi**) Proposed steps leading to HBV capsid nuclear import. The illustration was created using BioRender.

beam (cryo-FIB) milling (63) compared to previous NPC reconstructions obtained from purified nuclear envelopes. Similarly, cryo-ET analysis of cryo-FIB lamellae obtained from yeast NPC revealed that switching energy depletion to nutrients could also result in NPC dilation, which expands the inner ring to 69 nm (64). The cellular environment and sheer size of an import complex considerably influence NPC dimensions and architecture, made possible by the NPC's inherent plasticity (65). Thus, the current literature supports that the ~62-nm-wide HBV capsid fully decorated by 30 importin α1/β1 heterodimers can snugly translocate through a dilated NPC (Fig. 8, v). Several open questions remain as to the fate of HBV at the NPC basket, likely at Nup153, which makes high-affinity binding with importin β1 (Fig. 8, vi) (66). HBV is one of the rare cargos found to arrest at Nup153 (67).

In summary, we have deciphered how human importins recognize the HBV core. The exact spatial arrangements of the importin α1/β1 heterodimer with respect to the capsid could not be defined at atomic resolution due to HBV's unique NLS exposure mechanism. Each of the 30 quasi-sixfold pores exposes only one of six available NLSs, suggesting that our EC:Imp α1/β1 reconstruction is an average of up to 6^{30} possible HBV-NLSs bound to importin α1. In addition, the linker connecting importin α1 Arm core to importin β1 is highly flexible, as previously probed by limited proteolysis (47), preventing meaningful alignment of importin β1 tethered to the HBV NLS by importin α1. This flexibility makes it impossible to determine the exact importin α1/β1 quaternary structure, even after shortening the flexible linker in importin α1. The importin α1/β1 heterodimer built-in flexibility allows importin β1 to associate with phenylalanine-glycine nucleoporins and RanGTP during transport (68), promoting HBV nucleocapsid passage through the NPC channel. Despite HBV-NLS complexity and importins flexibility, combining structural and computational methods helped us define the association of importins with the HBV capsid with remarkable precision. Our work provides a logical framework to explain the role of phosphorylation in CTD that was previously observed but not explained in molecular terms.

MATERIALS AND METHODS
Biochemical methods
Expression plasmids encoding ΔIBB–Imp α1 (69), importin β1 (46), and importin α1/β1 complex (45) were expressed in bacteria and purified as previously described (fig. S1). Importin Δ53–76–α1 was generated by deletion polymerase chain reaction and coexpressed with importin β1, as described for the WT importin α1/β1 complex (45). MBP-α1 was generated by cloning ΔIBB–Imp α1 into an engineered pET28a(+) vector containing the MBP gene downstream of a 6×his-tag and purified as described for ΔIBB–Imp α1 (69). The genes encoding GST-CTD fusions, e.g., WT Cp183 CTD residues 150 to 178 (GST-WT-CTD), CTD lacking the NLS in Box4 (GST-ΔNLS-CTD), and CTD with three phosphomimetics at S155E, S162E, and S170E (GST-EEE-CTD), were chemically synthesized and cloned in a pGEX-6P (Novagen) expression plasmid. All expression plasmids were transformed into BL21 DE3 cells using electroporation. A single colony was picked and inoculated in 100 ml of LB medium and incubated at 37°C overnight. The enriched culture was amplified in 2 to 4 liters of LB medium and induced by 0.5 mM isopropyl-β-D-thiogalactopyranoside at 28°C for 3 hours. The cells were harvested by centrifuging at 4000 rpm for 20 min. Cells pellets were resuspended in lysis buffer [20 mM tris-HCl

(pH 8), 75 mM NaCl, 3 mM β-mercaptoethanol (BME), 1 mM phenylmethylsulfonyl fluoride] and homogenized by sonication. The lysate was centrifuged at 14,000 rpm for 30 min. Supernatants expressing his-tagged importins were combined with nickel agarose beads and incubated at 4°C for 2 hours. The beads were washed using wash buffer [20 mM tris-HCl (pH 8), 50 mM NaCl, and 5 mM Imidazole], and his-tagged importins were eluted by adding 10 ml of elution buffer [20 mM tris-HCl (pH 8), 50 mM NaCl, and 75 mM imidazole]. Untagged importin β1 was purified from the nickel immobilized importin α1/β1 complex as previously described (45). GST-CTD variants were purified on glutathione beads using a lysis buffer containing 0.1% Tween 20. All protein samples were further subjected to size exclusion chromatography on an ENrich SEC 650 column (Bio-Rad).

Purification of HBV ECs
Cp183 was overexpressed in bacteria as described (70). Bacterial RNA-filled capsids were disassociated to Cp183 dimers by overnight dialysis in disassembly buffer [1.5 M guanidine HCl, 0.5 M LiCl, 10 mM dithiothreitol (DTT), and 20 mM tris-HCL (pH 8)] at 4°C. Disassembled dimers were centrifuged at 13,000 rpm for 5 min, and the supernatant was subjected to ENrich SEC 650 equilibrated with disassembly buffer. All fractions at the peak representing Cp183 dimers were combined and dialyzed overnight in reassembly buffer [0.45 M NaCl, 10 mM DTT, and 20 mM tris-HCl (pH 8)]. Reassembled ECs were subjected to ENrich SEC 650 equilibrated with reassembly buffer (fig. S1). All fractions at the peak representing the ECs were combined and used for downstream assays.

Native agarose electrophoresis and pull-down binding assay
All samples used for native agarose electrophoresis were concentrated to at least 1 mg/ml, and the quantity of HBV ECs was fixed at 10 μg. After adding purified importins to EC, the mixture was incubated for 2 hours at 4°C and then analyzed on a 1.5% agarose gel. Native electrophoresis was performed in 0.5× TAMg buffer [20 mM tris base, 20 mM acetic acid, and 0.5 mM $MgSO_4$] at 100 V for 1 hour. The gel was then fixed in a fixing solution (25% isopropanol and 10% acetic acid) and washed three times in 95% ethanol. The gel was then dehydrated using a 583 gel dryer (Bio-Rad), stained by Brilliant Blue (Thermo Fisher Scientific), and destained by fixing solution. All gels were visualized using a Gel Doc XR+ (Bio-Rad). For the pull-down assay, purified GST-CTD variants were coupled to glutathione beads and incubated with 50 μl of 3 μM importin α1/β1. After 45 min of incubation, the beads were washed three times with 1× phosphate-buffered saline, and an equal amount of beads were analyzed by SDS-PAGE analysis. The experiment was repeated three times to estimate an SD.

Charge detection mass spectrometry
CD-MS allows mass distributions to be measured for heterogeneous samples that cannot be analyzed by conventional MS. It is a single-particle technique where the mass-to-charge ratio (m/z) and charge (z) of an ion are measured simultaneously. CD-MS instruments and methods have been described in detail elsewhere (71). This study was performed on a home-built instrument at Indiana University Bloomington. Briefly, ions are generated by nanoelectrospray and enter the instrument through a metal capillary. The ions are thermalized and pass through several differentially pumped regions before being focused into a dual hemispherical deflection

analyzer set to transmit ions with a nominal kinetic energy of 100 eV per charge. The ions are then focused into an electrostatic linear ion trap where trapped ions oscillate back and forth through a conducting cylinder. The induced charge from the oscillating ions is detected by a charge-sensitive amplifier. The resulting signal is analyzed by fast Fourier transforms. The *m/z* is determined from the fundamental frequency, while the charge is obtained from the magnitude. The product of the *m/z* and *z* gives the mass. Measurements are performed for thousands of individual ions and then binned into a mass histogram. The results can also be presented in a charge versus mass scatterplot. The plot can reveal correlations between charge and mass. The charge distribution can be used to infer information about the structure of the ions. Spherical ions are expected to have a charge close to the Rayleigh limit. Ions with more extended structures are expected to have higher charges (*72*).

Crystallographic methods

The peptide of Cp183 CTD was purchased from GenScript and dissolved to be a 5 mM solution. Purified mouse ΔIBB–Imp α1 was concentrated at 22 mg/ml. Hanging drop vapor diffusion was performed for crystal screening where 2 μl of protein was first mixed with 0.4 μl of peptide to reach a 1:2 mol ratio, then combined with 2.4 μl of the crystal solution [0.6 M sodium citrate, 0.1 M Hepes (pH 6.8 to 7.8), and 10 mM DTT], and equilibrated against 600 μl of reservoir. Crystals were harvested and cryoprotected with 27% ethylene glycol. The crystals were diffracted at the Stanford Synchrotron Radiation Lightsource (SSRL) using beamline 12-1. Data were indexed, integrated, and scaled using HKL2000 (*73*). Initial phases were obtained by molecular replacement using Phaser (*74*) and Protein Data Bank (PDB) 1Y2A as a search model. Detailed information about crystallographic x-ray data collection and model refinement are in Table 1.

Vitrification and data collection

The sample (2.5 μl) was applied to a 200-mesh copper Quantifoil R 2/1 holey carbon grid that had been negatively glow-discharged for 60 s at 15 mA in easiGlow (PELCO). All grids were blotted for 7 to 10 s at blot force 2 and frozen in liquid ethane using Vitrobot Mark IV (FEI). Micrographs were screened on 200-kV Glacios equipped with a Falcon 4 detector at Thomas Jefferson University. EPU software was used for data collection using accurate positioning mode. For high-resolution data collection, micrographs were collected on a Titan Krios microscope operated at 300 kV and equipped with a K3 (Gatan) or Falcon 4 (Thermo Fisher Scientific) direct electron detector camera at the National Cryo-EM Facility and National Center for Cryo-EM Access and Training (NCCAT), the National Cryo-EM Facility (NCEF) at NCI-Frederick National Laboratory, and Stanford-SLAC Cryo-EM Center (S^2C^2). A total of 10,015, 10,273, 6653, 8778, 13,570, and 2044 movies of EC, EC:ΔIBB–Imp α1, EC:Imp α1/β1, Imp α1/β1, EC:MBP-α1:antibody and EC:Imp Δ53–76–α1/β1 were collected, respectively. All cryo-EM data collection parameters are in Table 2 and table S1. The resolution of all reconstructions in this paper was estimated at an FSC of 0.143 (fig. S4).

Cryo-EM single-particle analysis

All movies were imported and analyzed by RELION (*75*). Motion correction was performed by RELION's implementation, and CTF estimation was done using CTFFIND-4.1 (*76*). An initial set of

particles were manually picked from 100 micrographs and used for an initial 2D classification. The best classes were chosen as templates for reference picking all micrographs. A second round of 2D classification was performed, and promising classes were selected for a 3D initial model and then set as the template for 3D classification. The best classes were selected for 3D autorefinement with icosahedral symmetry imposed for all capsid reconstructions, but no symmetry was applied for importin α1/β. For the EC:Imp α1/β map, the density was segmented using UCSF Chimera (*77*) to isolate the density for importin α1/β1. The extracapsid density at the center of the quasi-sixfold was picked and used as a template for mask creation in RELION (*75*). The mask was then used for 3D classification with no alignment and a regularization *T* value of 10. The 3D class with the highest resolution was used as a template for a second round of mask creation. A second round of no-alignment 3D classification was conducted using the latest mask and a regularization *T* value of 40. The 3D class with the best resolution was used for 3D autorefinement of the capsid complex, and the resulting map showed an arched density at the center. A detailed workflow of all cryo-EM SPA methods used to solve EC bound to importins is shown in fig. S3.

Experimental modeling

All models derived from crystallography and cryo-EM data were built using Coot (*78*) and refined using phenix.real_space_refine (*79*). The Cp183 dimer crystal structure (PDB: 1QGT) (*80*) was docked into the cryo-EM density and used to generate the icosahedral asymmetric unit. The complete HBV EC capsid was generated using UCSF Chimera (*77*). S155, S162, and S170 of Cp183 CTD were phosphorylated in silico using Coot (*81*). Atomic distances were measured using UCSF Chimera (*77*). IBB-bound importin β1 (PDB: 1QGK) (*46*) was used to measure the diameter of importin α1/β1–decorated capsid. All ribbon diagrams and surface representations were generated using UCSF Chimera (*77*), Chimera X (*82*), and PyMOL (*83*).

Computational modeling

HBV CTD simulation models are based on strain adyw (UniProtKB accession code P03147.1) and encompass residues 150 to 183. Initial CTD conformations for the unphosphorylated and phosphate-containing systems were predicted de novo with ROSETTA (*81, 84*), using phosphomimetic glutamates for the latter. Fragment files and secondary structure predictions were produced using Robetta (*85*). An ensemble of 10,000 candidate conformations was generated for each system. Following ab initio folding, the structures were relaxed using the fast relax protocol. The combinatorial averaged transient structure clustering algorithm for intrinsically disordered peptides was used to cluster each ensemble based on φ/ψ backbone torsions (*86*). Clusters were relaxed using a population cutoff α of 100, corresponding to 1.0% of the ensemble. The number of ignorable coordinates β was set to 10, corresponding to ~15% of the structural descriptor. The top 100 clusters were selected using an ε value of 1.0. The representative structures of the top three most populated clusters from each ensemble were selected for MD simulation. Phosphomimetic glutamates were substituted with phosphoserine. Local ions were placed around the CTD models using CIonize in visual MD (VMD) (*87*). The systems were each immersed in an 88-$Å^3$ solvent box containing 21,252 water molecules and neutralized in a salt concentration of 150 mM NaCl. Simulation input files were prepared with psfgen in VMD, applying the CHARMM36m force field

(88) and TIP3P water parameters (89). Thus, the initial states for three independent simulations were prepared for both the unphosphorylated and S150-, S162-, and S170-phosphorylated systems.

Models of the importin α1:HBV-NLS complexes were constructed on the basis of the crystal structure reported here. Simulation input files were prepared with psfgen in VMD, then converted to AMBER-compatible formats using ParmEd from AmberTools 22 (90). Local ions were placed around the complexes using CIonize in VMD. The systems were immersed in 115-Å^3 solvent boxes and neutralized in a salt concentration of 150 mM NaCl. NLS peptide termini were assigned neutral charges. Systems were described with the CHARMM36m force field (88) and TIP3P water parameters (89). Thus, the initial states were prepared for two simulations, each run in triplicate for unphosphorylated (WT) and phosphate modification at S170, respectively.

MD simulations

Equilibration of the isolated CTD systems was performed using NAMD 2.14 (91). All MD simulations of the α1:HBV-NLS complexes were performed using AMBER 22 pmemd.cuda (90). Each system was subjected to energy minimization using the steepest descent algorithm for 2000 cycles, first for the solvent and then for the protein side chains. The systems were heated gradually from 60 to 310 K, increasing the temperature by 5 K at intervals of 100 ps. Cartesian backbone restraints of 5 kcal/mol were gradually released over an additional period of 5 ns. Each isolated CTD system was equilibrated for 50 ns in the isothermal-isobaric ensemble, followed by 20 ns in the canonical ensemble before transfer to Anton 2. The α1:HBV-NLS complexes were equilibrated for 200 ns in the isothermal-isobaric ensemble, followed by production runs of 400 ns. Each simulation was performed in triplicate.

NAMD 2.14 and AMBER 22 simulations used an integration time step of 2 fs. Bonds involving hydrogens were constrained with the SHAKE algorithm. A cutoff of 12 Å was used to split short- and long-range electrostatic interactions. The particle-mesh Ewald algorithm was used to compute long-range electrostatics with a grid spacing of 1.0 Å. The temperature was controlled at a target of 310 K with the Langevin thermostat algorithm, using a damping coefficient of 1.0 ps^{-1}. The pressure was controlled at a target of 1.0 bar either with the Nosé-Hoover Langevin piston algorithm, using a piston oscillation period of 200 fs and damping timescale of 100 fs (NAMD 2.14), or with the Berendsen algorithm, using a pressure relaxation time of 1 ps (AMBER 22).

Production MD simulations of the isolated CTDs were performed on the Anton 2 special purpose computer using the simulated tempering method (92). The temperature ladder ranged from 310 to 330 K, with rungs at intervals of 1 K. Rung weights were determined using the approach proposed by Park and Pande (93). Simulations were performed for 10 μs each in a mixed-canonical ensemble using an integration time step of 2.5 fs.

MD trajectory analysis

Analysis of MD simulation trajectories, including the calculation of the radius of gyration (Rg), peptide end-to-end peptide distance, SASA, hydrogen bonds, and salt bridges, was carried out with VMD. Data from three independent simulations were combined for each system. The minimum NLS SASA required for binding of importin α1/β was estimated on the basis of the structure of ΔIBB–Imp α1:HBV-NLS complex by subtracting the SASA of the

bound NLS from that of the unbound NLS in its crystallographic conformation.

Binding free energies for the α1:HBV-NLS complexes were calculated using the molecular mechanics/generalized Born surface area method (50), as implemented in MMPBSA.py from AmberTools22. The GB model (igb = 5) corresponds to that developed by Onufriev et al. (94), and molecular radii were taken from the mbondi2 set. A salt concentration of 150 mM and a surface tension of 0.00072 kcal/mol per Å^2 were used. Surface area for the nonpolar contribution was calculated using linear combination of pairwise overlaps method.

Supplementary Materials

This PDF file includes:
Figs. S1 to S10
Table S1
References

REFERENCES AND NOTES

1. T. M. Block, K. M. Chang, J. T. Guo, Prospects for the global elimination of hepatitis B. *Annu. Rev. Virol.* **8**, 437–458 (2021).
2. Y. Shi, M. Zheng, Hepatitis B virus persistence and reactivation. *BMJ* **370**, m2200 (2020).
3. S. Tsukuda, K. Watashi, Hepatitis B virus biology and life cycle. *Antiviral Res.* **182**, 104925 (2020).
4. J. Tian, C. Li, W. Li, Entry of hepatitis B virus: Going beyond NTCP to the nucleus. *Curr. Opin. Virol.* **50**, 97–102 (2021).
5. B. Venkatakrishnan, A. Zlotnick, The structural biology of hepatitis B virus: Form and function. *Annu. Rev. Virol.* **3**, 429–451 (2016).
6. L. B. Rall, D. N. Standring, O. Laub, W. J. Rutter, Transcription of hepatitis B virus by RNA polymerase II. *Mol. Cell. Biol.* **3**, 1766–1773 (1983).
7. C. T. Yeh, Y. F. Liaw, J. H. Ou, The arginine-rich domain of hepatitis B virus precore and core proteins contains a signal for nuclear transport. *J. Virol.* **64**, 6141–6147 (1990).
8. S. G. Eckhardt, D. R. Milich, A. McLachlan, Hepatitis B virus core antigen has two nuclear localization sequences in the arginine-rich carboxyl terminus. *J. Virol.* **65**, 575–582 (1991).
9. A. S. Aris Haryanto, B. Rabe, E. Gassert, A. Vlachou, M. Kann, Analysis of the nuclear localization signal of the hepatitis B virus capsid. *Int. Res. J. Biochem. Bioinform.* **2**, 174–185 (2012).
10. M. Kann, B. Sodeik, A. Vlachou, W. H. Gerlich, A. Helenius, Phosphorylation-dependent binding of hepatitis B virus core particles to the nuclear pore complex. *J. Cell Biol.* **145**, 45–55 (1999).
11. B. Rabe, A. Vlachou, N. Pante, A. Helenius, M. Kann, Nuclear import of hepatitis B virus capsids and release of the viral genome. *Proc. Natl. Acad. Sci. U. S. A.* **100**, 9849–9854 (2003).
12. H. de Rocquigny, V. Rat, F. Pastor, J. L. Darlix, C. Hourioux, P. Roingeard, Phosphorylation of the arginine-rich C-terminal domains of the hepatitis B virus (HBV) core protein as a fine regulator of the interaction between HBc and nucleic acid. *Viruses* **12**, 738 (2020).
13. L. Selzer, R. Kant, J. C. Wang, B. Bothner, A. Zlotnick, Hepatitis B virus core protein phosphorylation sites affect capsid stability and transient exposure of the C-terminal domain. *J. Biol. Chem.* **290**, 28584–28593 (2015).
14. E. V. Gazina, J. E. Fielding, B. Lin, D. A. Anderson, Core protein phosphorylation modulates pregenomic RNA encapsidation to different extents in human and duck hepatitis B viruses. *J. Virol.* **74**, 4721–4728 (2000).
15. B. Beames, R. E. Lanford, Carboxy-terminal truncations of the HBV core protein affect capsid formation and the apparent size of encapsidated HBV RNA. *Virology* **194**, 597–607 (1993).
16. M. Nassal, The arginine-rich domain of the hepatitis B virus core protein is required for pregenome encapsidation and productive viral positive-strand DNA synthesis but not for virus assembly. *J. Virol.* **66**, 4107–4116 (1992).
17. W. Liao, J. H. Ou, Phosphorylation and nuclear localization of the hepatitis B virus core protein: Significance of serine in the three repeated SPRRR motifs. *J. Virol.* **69**, 1025–1029 (1995).
18. Y. T. Lan, J. Li, W. Liao, J. Ou, Roles of the three major phosphorylation sites of hepatitis B virus core protein in viral replication. *Virology* **259**, 342–348 (1999).
19. S. Le Pogam, P. K. Chua, M. Newman, C. Shih, Exposure of RNA templates and encapsidation of spliced viral RNA are influenced by the arginine-rich domain of human hepatitis B virus core antigen (HBcAg 165-173). *J. Virol.* **79**, 1871–1887 (2005).
20. S. H. Basagoudanavar, D. H. Perlman, J. Hu, Regulation of hepadnavirus reverse transcription by dynamic nucleocapsid phosphorylation. *J. Virol.* **81**, 1641–1649 (2007).

21. P. Y. Su, C. J. Yang, T. H. Chu, C. H. Chang, C. Chiang, F. M. Tang, C. Y. Lee, C. Shih, HBV maintains electrostatic homeostasis by modulating negative charges from phosphoserine and encapsidated nucleic acids. *Sci. Rep.* **6**, 38959 (2016).

22. Q. Zhao, Z. Hu, J. Cheng, S. Wu, Y. Luo, J. Chang, J. Hu, J. T. Guo, Hepatitis B virus core protein dephosphorylation occurs during pregenomic RNA encapsidation. *J. Virol.* **92**, e02139–e02117 (2018).

23. A. Diab, A. Foca, F. Zoulim, D. Durantel, O. Andrisani, The diverse functions of the hepatitis B core/capsid protein (HBc) in the viral life cycle: Implications for the development of HBc-targeting antivirals. *Antiviral Res.* **149**, 211–220 (2018).

24. C. Chen, J. C. Wang, A. Zlotnick, A kinase chaperones hepatitis B virus capsid assembly and captures capsid dynamics in vitro. *PLoS Pathog.* **7**, e1002388 (2011).

25. Y. Zheng, X. D. Fu, J. H. Ou, Suppression of hepatitis B virus replication by SRPK1 and SRPK2 via a pathway independent of the phosphorylation of the viral core protein. *Virology* **342**, 150–158 (2005).

26. L. Ludgate, X. Ning, D. H. Nguyen, C. Adams, L. Mentzer, J. Hu, Cyclin-dependent kinase 2 phosphorylates s/t-p sites in the hepadnavirus core protein C-terminal domain and is incorporated into viral capsids. *J. Virol.* **86**, 12237–12250 (2012).

27. A. E. Elia, P. Rellos, L. F. Haire, J. W. Chao, F. J. Ivins, K. Hoepker, D. Mohammad, L. C. Cantley, S. J. Smerdon, M. B. Yaffe, The molecular basis for phosphodependent substrate targeting and regulation of Plks by the Polo-box domain. *Cell* **115**, 83–95 (2003).

28. A. Diab, A. Foca, F. Fusil, T. Lahlali, P. Jalaguier, F. Amirache, L. N'Guyen, N. Isorce, F. L. Cosset, F. Zoulim, O. Andrisani, D. Durantel, Polo-like-kinase 1 is a proviral host factor for hepatitis B virus replication. *Hepatology* **66**, 1750–1765 (2017).

29. Z. Hu, H. Ban, H. Zheng, M. Liu, J. Chang, J. T. Guo, Protein phosphatase 1 catalyzes HBV core protein dephosphorylation and is co-packaged with viral pregenomic RNA into nucleocapsids. *PLOS Pathog.* **16**, e1008669 (2020).

30. T. H. Chu, T. Liou, P. Y. Su, H. N. Wu, C. Shih, Nucleic acid chaperone activity associated with the arginine-rich domain of human hepatitis B virus core protein. *J. Virol.* **88**, 2530–2543 (2014).

31. I. G. Macara, Transport into and out of the nucleus. *Microbiol. Mol. Biol. Rev.* **65**, 570–594 (2001).

32. M. Stewart, Molecular mechanism of the nuclear protein import cycle. *Nat. Rev. Mol. Cell Biol.* **8**, 195–208 (2007).

33. M. Marfori, A. Mynott, J. J. Ellis, A. M. Mehdi, N. F. Saunders, P. M. Curmi, J. K. Forwood, M. Boden, B. Kobe, Molecular basis for specificity of nuclear import and prediction of nuclear localization. *Biochim. Biophys. Acta* **1813**, 1562–1577 (2011).

34. R. A. Pumroy, G. Cingolani, Diversification of importin-α isoforms in cellular trafficking and disease states. *Biochem. J.* **466**, 13–28 (2015).

35. K. Lott, G. Cingolani, The importin β binding domain as a master regulator of nucleocytoplasmic transport. *Biochim. Biophys. Acta* **1813**, 1578–1592 (2011).

36. S. J. Lee, Y. Matsuura, S. M. Liu, M. Stewart, Structural basis for nuclear import complex dissociation by RanGTP. *Nature* **435**, 693–696 (2005).

37. G. Paci, T. Zheng, J. Caria, A. Zilman, E. A. Lemke, Molecular determinants of large cargo transport into the nucleus. *eLife* **9**, e55963 (2020).

38. N. Fay, N. Pante, Nuclear entry of DNA viruses. *Front. Microbiol.* **6**, 467 (2015).

39. V. Zila, E. Margiotta, B. Turonova, T. G. Muller, C. E. Zimmerli, S. Mattei, M. Allegretti, K. Borner, J. Rada, B. Muller, M. Lusic, H. G. Krausslich, M. Beck, Cone-shaped HIV-1 capsids are transported through intact nuclear pores. *Cell* **184**, 1032–1046.e18 (2021).

40. J. D. Nardozzi, K. Lott, G. Cingolani, Phosphorylation meets nuclear import: A review. *Cell Commun. Signal* **8**, 32 (2010).

41. C. Chen, J. C. Wang, E. E. Pierson, D. Z. Keifer, M. Delaleau, L. Gallucci, C. Cazenave, M. Kann, M. F. Jarrold, A. Zlotnick, Importin β can bind hepatitis b virus core protein and empty core-like particles and induce structural changes. *PLoS Pathog.* **12**, e1005802 (2016).

42. K. Lott, A. Bhardwaj, G. Mitrousis, N. Pante, G. Cingolani, The importin beta binding domain modulates the avidity of importin beta for the nuclear pore complex. *J. Biol. Chem.* **285**, 13769–13780 (2010).

43. A. R. Todd, L. F. Barnes, K. Young, A. Zlotnick, M. F. Jarrold, Higher resolution charge detection mass spectrometry. *Anal. Chem.* **92**, 11357–11364 (2020).

44. C. Kim, C. J. Schlicksup, C. Perez-Segura, J. A. Hadden-Perilla, J. C. Wang, A. Zlotnick, Structure of the hepatitis B virus capsid quasi-6-fold with a trapped C-terminal domain reveals capsid movements associated with domain exit. *J. Biol. Chem.* **299**, 105104 (2023).

45. S. G. Doll, H. Meshkin, A. J. Bryer, F. Li, Y. H. Ko, R. K. Lokareddy, R. E. Gillilan, K. Gupta, J. R. Perilla, G. Cingolani, Recognition of the TDP-43 nuclear localization signal by importin α1/β. *Cell Rep.* **39**, 111007 (2022).

46. G. Cingolani, C. Petosa, K. Weis, C. W. Muller, Structure of importin-β bound to the IBB domain of importin-α. *Nature* **399**, 221–229 (1999).

47. G. Cingolani, H. A. Lashuel, L. Gerace, C. W. Muller, Nuclear import factors importin alpha and importin beta undergo mutually induced conformational changes upon association. *FEBS Lett.* **484**, 291–298 (2000).

48. J. Pugh, A. Zweidler, J. Summers, Characterization of the major duck hepatitis B virus core particle protein. *J. Virol.* **63**, 1371–1376 (1989).

49. D. H. Perlman, E. A. Berg, B. O'Connor, C. E. Costello, J. Hu, Reverse transcription-associated dephosphorylation of hepadnavirus nucleocapsids. *Proc. Natl. Acad. Sci. U.S.A.* **102**, 9020–9025 (2005).

50. G. Rastelli, A. Del Rio, G. Degliesposti, M. Sgobba, Fast and accurate predictions of binding free energies using MM-PBSA and MM-GBSA. *J. Comput. Chem.* **31**, 797–810 (2010).

51. J. Hu, C. Seeger, Hepadnavirus genome replication and persistence. *Cold Spring Harb. Perspect. Med.* **5**, a021386 (2015).

52. R. Prange, Hepatitis B virus movement through the hepatocyte: An update. *Biol. Cell* **114**, 325–348 (2022).

53. R. E. Lanford, L. Notvall, Expression of hepatitis B virus core and precore antigens in insect cells and characterization of a core-associated kinase activity. *Virology* **176**, 222–233 (1990).

54. J. M. Hogle, Poliovirus cell entry: Common structural themes in viral cell entry pathways. *Annu. Rev. Microbiol.* **56**, 677–702 (2002).

55. J. K. Lewis, J. Bothner, T. J. Smith, G. Siuzdak, Antiviral agent blocks breathing of the common cold virus. *Proc. Natl. Acad. Sci. U.S.A.* **95**, 6774–6778 (1998).

56. K. A. Dowd, T. C. Pierson, The many faces of a dynamic virion: Implications of viral breathing on flavivirus biology and immunogenicity. *Annu. Rev. Virol.* **5**, 185–207 (2018).

57. S. Bajaj, D. Dey, R. Bhukar, M. Kumar, M. Banerjee, Non-enveloped virus entry: Structural determinants and mechanism of functioning of a viral lytic peptide. *J. Mol. Biol.* **428**, 3540–3556 (2016).

58. M. Callon, A. A. Malar, L. Lecoq, M. Dujardin, M. L. Fogeron, S. Wang, M. Schledorn, T. Bauer, M. Nassal, A. Bockmann, B. H. Meier, Fast magic-angle-spinning NMR reveals the evasive hepatitis B virus capsid C-terminal domain**. *Angew. Chem. Int. Ed. Engl.* **61**, e202201083 (2022).

59. G. Riddick, I. G. Macara, A systems analysis of importin-{alpha}-{beta} mediated nuclear protein import. *J. Cell Biol.* **168**, 1027–1038 (2005).

60. B. L. Timney, J. Tetenbaum-Novatt, D. S. Agate, R. Williams, W. Zhang, B. T. Chait, M. P. Rout, Simple kinetic relationships and nonspecific competition govern nuclear import rates in vivo. *J. Cell Biol.* **175**, 579–593 (2006).

61. C. Albin, W. S. Robinson, Protein kinase activity in hepatitis B virus. *J. Virol.* **34**, 297–302 (1980).

62. Q. Shen, C. Wu, C. Freniere, T. N. Tripler, Y. Xiong, Nuclear import of HIV-1. *Viruses* **13**, 2242 (2021).

63. A. P. Schuller, M. Wojtynek, D. Mankus, M. Tatli, R. Kronenberg-Tenga, S. G. Regmi, P. V. Dip, A. K. R. Lytton-Jean, E. J. Brignole, M. Dasso, K. Weis, O. Medalia, T. U. Schwartz, The cellular environment shapes the nuclear pore complex architecture. *Nature* **598**, 667–671 (2021).

64. M. Allegretti, C. E. Zimmerli, V. Rantos, F. Wilfling, P. Ronchi, H. K. H. Fung, C. W. Lee, W. Hagen, B. Turonova, K. Karius, M. Bormel, X. Zhang, C. W. Muller, Y. Schwab, J. Mahamid, B. Pfander, J. Kosinski, M. Beck, In-cell architecture of the nuclear pore and snapshots of its turnover. *Nature* **586**, 796–800 (2020).

65. S. Petrovic, D. Samanta, T. Perriches, C. J. Bley, K. Thierbach, B. Brown, S. Nie, G. W. Mobbs, T. A. Stevens, X. Liu, G. P. Tomaleri, L. Schaus, A. Hoelz, Architecture of the linker-scaffold in the nuclear pore. *Science* **376**, eabm9798 (2022).

66. A. R. Lowe, J. H. Tang, J. Yassif, M. Graf, W. Y. Huang, J. T. Groves, K. Weis, J. T. Liphardt, Importin-β modulates the permeability of the nuclear pore complex in a Ran-dependent manner. *eLife* **4**, e04052 (2015).

67. A. Schmitz, A. Schwarz, M. Foss, L. Zhou, B. Rabe, J. Hoellenriegel, M. Stoeber, N. Pante, M. Kann, Nucleoporin 153 arrests the nuclear import of hepatitis B virus capsids in the nuclear basket. *PLoS Pathog.* **6**, e1000741 (2010).

68. R. Bayliss, T. Littlewood, M. Stewart, Structural basis for the interaction between FxFG nucleoporin repeats and importin-beta in nuclear trafficking. *Cell* **102**, 99–108 (2000).

69. R. S. Sankhala, R. K. Lokareddy, S. Begum, R. A. Pumroy, R. E. Gillilan, G. Cingolani, Three-dimensional context rather than NLS amino acid sequence determines importin α subtype specificity for RCC1. *Nat. Commun.* **8**, 979 (2017).

70. C. Kim, L. F. Barnes, C. J. Schlicksup, A. J. Patterson, B. Bothner, M. F. Jarrold, J. C. Wang, A. Zlotnick, Core protein-directed antivirals and importin β can synergistically disrupt hepatitis B virus capsids. *J. Virol.* **96**, e0139521 (2022).

71. M. F. Jarrold, Applications of charge detection mass spectrometry in molecular biology and biotechnology. *Chem. Rev.* **122**, 7415–7441 (2022).

72. L. Konermann, E. Ahadi, A. D. Rodriguez, S. Vahidi, Unraveling the mechanism of electrospray ionization. *Anal. Chem.* **85**, 2–9 (2013).

73. Z. Otwinowski, W. Minor, Processing of x-ray diffraction data collected in oscillation mode. *Methods Enzymol.* **276**, 307–326 (1997).

74. P. Evans, A. McCoy, An introduction to molecular replacement. *Acta Crystallogr. D Biol. Crystallogr.* **64**, 1–10 (2008).

75. S. H. Scheres, RELION: Implementation of a Bayesian approach to cryo-EM structure determination. *J. Struct. Biol.* **180**, 519–530 (2012).

76. A. Rohou, N. Grigorieff, CTFFIND4: Fast and accurate defocus estimation from electron micrographs. *J. Struct. Biol.* **192**, 216–221 (2015).

77. E. F. Pettersen, T. D. Goddard, C. C. Huang, G. S. Couch, D. M. Greenblatt, E. C. Meng, T. E. Ferrin, UCSF chimera—A visualization system for exploratory research and analysis. *J. Comput. Chem.* **25**, 1605–1612 (2004).

78. P. Emsley, K. Cowtan, Coot: Model-building tools for molecular graphics. *Acta Crystallogr. D Biol. Crystallogr.* **60**, 2126–2132 (2004).

79. P. V. Afonine, B. K. Poon, R. J. Read, O. V. Sobolev, T. C. Terwilliger, A. Urzhumtsev, P. D. Adams, Real-space refinement in PHENIX for cryo-EM and crystallography. *Acta Crystallogr. D Struct. Biol.* **74**, 531–544 (2018).

80. S. A. Wynne, R. A. Crowther, A. G. Leslie, The crystal structure of the human hepatitis B virus capsid. *Mol. Cell* **3**, 771–780 (1999).

81. C. A. Rohl, C. E. Strauss, K. M. Misura, D. Baker, Protein structure prediction using Rosetta. *Methods Enzymol.* **383**, 66–93 (2004).

82. T. D. Goddard, C. C. Huang, E. C. Meng, E. F. Pettersen, G. S. Couch, J. H. Morris, T. E. Ferrin, UCSF ChimeraX: Meeting modern challenges in visualization and analysis. *Protein Sci.* **27**, 14–25 (2018).

83. W. L. DeLano, The PyMOL molecular graphics system version 1.8 (Schrödinger LLC. 2002).

84. A. Leaver-Fay, M. Tyka, S. M. Lewis, O. F. Lange, J. Thompson, R. Jacak, K. Kaufman, P. D. Renfrew, C. A. Smith, W. Sheffler, I. W. Davis, S. Cooper, A. Treuille, D. J. Mandell, F. Richter, Y. E. Ban, S. J. Fleishman, J. E. Corn, D. E. Kim, S. Lyskov, M. Berrondo, S. Mentzer, Z. Popovic, J. J. Havranek, J. Karanicolas, R. Das, J. Meiler, T. Kortemme, J. J. Gray, B. Kuhlman, D. Baker, P. Bradley, ROSETTA3: An object-oriented software suite for the simulation and design of macromolecules. *Methods Enzymol.* **487**, 545–574 (2011).

85. D. E. Kim, D. Chivian, D. Baker, Protein structure prediction and analysis using the Robetta server. *Nucleic Acids Res.* **32**, W526–W531 (2004).

86. J. C. Ezerski, M. S. Cheung, CATS: A tool for clustering the ensemble of intrinsically disordered peptides on a flat energy landscape. *J. Phys. Chem. B* **122**, 11807–11816 (2018).

87. W. Humphrey, A. Dalke, K. Schulten, VMD: Visual molecular dynamics. *J. Mol. Graph.* **14**, 27–28 (1996).

88. J. Huang, S. Rauscher, G. Nawrocki, T. Ran, M. Feig, B. L. de Groot, H. Grubmuller, A. D. MacKerell Jr., CHARMM36m: An improved force field for folded and intrinsically disordered proteins. *Nat. Methods* **14**, 71–73 (2017).

89. L. W. Jorgensen, J. Chandrasekhar, D. J. Madura, W. R. Impey, L. M. Klein, Comparison of simple potential functions for simulating liquid water. *J. Chem. Phys.* **79**, 926–935 (1983).

90. D. A. Case, H. M. Aktulga, K. Belfon, J. I. Y. Ben-Shalom, .T. Berryman, S. R. Brozell, D. S. Cerutti, I. T. E. Cheatham, G. A. Cisneros, V. W. D. Cruzeiro, T. A. Darden, R. E. Duke, G. Giambaşu, T. Giese, M. K. Gilson, H. Gohlke, A. W. Goetz, J. Harris, S. Izadi, S. A. Izmailov, K. Kasavajhala, M. C. Kaymak, E. King, A. Kovalenko, T. Kurtzman, T. S. Lee, P. Li, C. Lin, J. Liu, T. Luchko, R. Luo, M. Machado, V. Man, M. Manathunga, K. M. Merz, Y. Miao, O. Mikhailovskii, G. Monard, H. Nguyen, K. A. O'Hearn, A. Onufriev, F. Pan, S. Pantano, R. Qi, A. Rahnamoun, D. R. Roe, A. Roitberg, C. Sagui, S. Schott-Verdugo, A. Shajan, J. Shen, N. C. L. Simmerling, .R. Skrynnikov, J. Smith, J. Swails, R. C. Walker, J. Wang, J. Wang, H. Wei, X. Wu, X. Xiong, Y. Xue, D. M. York, S. Zhao, Q. Zhu, P. A. Kollman, Amber 2023. University of California, San Francisco (2023).

91. J. C. Phillips, R. Braun, W. Wang, J. Gumbart, E. Tajkhorshid, E. Villa, C. Chipot, R. D. Skeel, L. Kale, K. Schulten, Scalable molecular dynamics with NAMD. *J. Comput. Chem.* **26**, 1781–1802 (2005).

92. A. C. Pan, T. M. Weinreich, S. Piana, D. E. Shaw, Demonstrating an order-of-magnitude sampling enhancement in molecular dynamics simulations of complex protein systems. *J. Chem. Theory Comput.* **12**, 1360–1367 (2016).

93. S. Park, V. S. Pande, Choosing weights for simulated tempering. *Phys. Rev. E Stat. Nonlin. Soft Matter Phys.* **76**, 016703 (2007).

94. A. Onufriev, D. Bashford, D. A. Case, Exploring protein native states and large-scale conformational changes with a modified generalized born model. *Proteins* **55**, 383–394 (2004).

95. M. D. Abramoff, P. J. Magelhaes, S. J. Ram, Image processing with ImageJ. *Biophotonics Int.* **11**, 36–42 (2004).